

**Università degli Studi di Modena e Reggio Emilia**

DIPARTIMENTO DI INGEGNERIA “ENZO FERRARI”

CORSO DI LAUREA MAGISTRALE IN INGEGNERIA INFORMATICA

---

## **Inferior Alveolar Canal Segmentation using Deep Neural Networks**

---

*Relatore:*

*Candidato:*

Luca Lumetti

Prof. Costantino Grana

*Correlatore:*

Prof. Federico Bolelli

ANNO ACCADEMICO 2021-2022

# *Abstract*

## **Inferior Alveolar Canal Segmentation using Deep Neural Networks**

Dental implant placement within the jawbone is a routinely executed surgical procedure, which can become complex due to the local presence of the Inferior Alveolar Nerve (IAN). In particular, the nerve is oftentimes in close relation to the roots of molars, and its position must thus be carefully detailed before the surgical removal. As avoiding contact with the IAN is a primary concern during these operations, segmentation plays a key role in surgical preparations.

Unfortunately, 3D manual segmentation requires a huge amount of time to be carried out, thus perfect anatomical annotations are usually overlooked in favor of fast executions. The de facto standard in radiology medical centers for dentistry and maxilla facial purposes is based on sparse annotations, which can be obtained from 2D images in a relatively small amount of time. This type of annotation fails to identify a considerable amount of inner information about the IAN position and the bone structure. Convolutional Neural Networks are known to provide amazing results in the segmentation task and could provide to medical operators an automatic and precise way to detect the IAN in patients, allow them to be more accurate during the operations where this information is critical. This type of network requires a large amount of labeled data to reach a good level of accuracy while in the medical field is hard and expensive to acquire, meanwhile a good amount of unlabeled data is available.

In this work we study and analyze the effectiveness of some of the most recent proposal made in the literature for segmentation in the medical imaging field, some of which have recently obtained state-of-the-art results for other similar tasks. Even if we do not reach the same level of accuracy we expected, we show that we were able to improve the speed of the training process and the performance of the network, while keeping the same level of accuracy of the original network.

**Keywords:** Medical Imaging, Deep Learning, 3D Segmentation, Computer Vision, Cone Beam Computed Tomography.

## *Abstract in Italian*

### **Utilizzo di Reti Neurali per la Segmentazione del Canale Alveolare Inferiore**

L'inserimento di impianti dentali nella mascella è una routine chirurgica abbastanza comune, ma è resa non banale dalla presenza del nervo alveolare inferiore. Questo nervo è posizionato in prossimità delle radici dei molari, e la sua posizione deve essere accuratamente delineata prima di poter eseguire l'operazione voluta, in quanto danneggiare tale nervo potrebbe essere causa di gravi conseguenze per il paziente, come ad esempio la perdita della sensibilità o la paralisi di tale zona. Poichè evitare il contatto con questo nervo è essenziale, un'accurata segmentazione di tale nervo è un requisito chiave. Sfortunatamente, una segmentazione 3D manuale richiede un'enorme quantità di tempo, per questo motivo solitamente si preferiscono metodi meno precisi ma più veloci e per questo motivo lo standard de-facto per i dentisti è basato sull'effettuare una annotazione sparsa, ottenuta da immagini 2D. Questo tipo di annotazione fallisce nell'identificare una buona parte delle informazioni che riguardano la posizione del nervo e la struttura ossea del canale in cui esso è contenuto.

Le reti neurali convolutive hanno dimostrato di poter ottenere risultati ottimi nell'effettuare la segmentazione di immagini e in questo caso potrebbe offrire ai medici un metodo automatico, preciso e veloce di delineare il nervo alveolare inferiore, essenziale soprattutto durante le operazioni più critiche. Questo tipo di reti neurali richiede una quantità enorme di dati annotati per poter imparare a svolgere correttamente questo tipo di task con una accuratezza soddisfacente. In ambito medico, è possibile ottenere una decente quantità di immagini, ma non di annotazioni. Per questo motivo è necessario progettare accuratamente i metodi utilizzati durante il design e l'allenamento di tali reti in modo da superare questa mancanza senza perdere in prestazioni. In questa tesi, diverse tecniche molto recenti vengono provate ed analizzate, per studiarne l'efficacia in questo specifico lavoro. Alcuni metodi che recentemente hanno avuto molto successo nell'ambito della computer vision, non hanno avuto gli stessi risultati sperati in questo specifico caso, mentre altri approcci si sono rivelati molto efficaci nell'ottimizzare e velocizzare il processo di training della rete, senza perdere accuratezza nella segmentazione.

**Parole Chiave:** Medical Imaging, Deep Learning, 3D Segmentation, Computer Vision, Cone Beam Computed Tomography.

## *Summary in Italian*

Il regolamento della Facoltà di Ingegneria di Modena prevede che le tesi scritte in lingua inglese debbano contenere un *abstract* ed un’ampia sintesi dei contenuti in lingua italiana: in accordo a questa regola, proponiamo un sunto degli argomenti, delle tecniche e dei risultati che verranno delineati nell’elaborato. Si noti che non si tratta di un sunto esaustivo, e che non è possibile valutare la tesi dalla semplice lettura di queste righe. Per una descrizione più dettagliata e più rigorosa, e per i risultati sperimentali ottenuti, si rimanda al testo in inglese.

Questa tesi tratta della segmentazione del canale alveolare inferiore su immagini di tomografia conica a fascio di coni (Cone Beam Computed Tomography, CBCT) tramite l’utilizzo di reti neurali. Tale procedura è essenziale per l’inserimento di impianti dentali nella mascella, poichè il nervo alveolare inferiore deve essere accuratamente delineato prima di poter eseguire l’operazione voluta, in quanto danneggiare tale nervo potrebbe essere causa di gravi conseguenze per il paziente, come ad esempio la perdita della sensibilità o la paralisi di tale zona.

La segmentazione di immagini è un problema di grande interesse in ambito della visione artificiale, in quanto permette di ottenere informazioni utili per diversi scopi. In ambito medico, la segmentazione di immagini risulta uno strumento molto utile a supporto dei medici. Per questo motivo c’è stata una forte ricerca sulla segmentazione di immagini mediche (CT, CBCT, MRI, ecc.), che ha seguito i trend della visione artificiale ”classica”. Ad oggi, quest’area è dominata dalle reti neurali, che hanno dimostrato di poter ottenere risultati molto migliori delle tecniche classiche. Negli ultimi anni, la tipologia di reti neurali che ha avuto maggior successo è stata quella delle reti neurali completamente convolutive (CNN), ovvero reti neurali che non hanno alcun layer completamente connesso ma solo layer convoluzionali. Tra queste, si è visto che le reti a forma di U, come U-Net, sono quelle che ottengono i migliori risultati, dato dal fatto che sono in grado di essere molto profonde senza soffrire del problema del gradiente evanescente grazie alle connessioni residuali. Queste reti seguono un approccio di codifica-decodifica, in cui l’input viene codificato in una rappresentazione più compatta, che viene successivamente decodificata in un output di dimensione equivalente a quella di input.

Negli ultimi anni però i transformers, un tipo di rete neurale che sfrutta la tecnica dell’attenzione proposto per la prima volta nel campo del linguaggio naturale, hanno ottenuto risultati molto interessanti anche nell’ambito delle immagini. Non sono stati fin da subito adottati anche

nel campo medico perché hanno la scomoda caratteristica di aver bisogno di molti dati per ottenere risultati comparabili o superiori alle reti convolutive. I dataset di immagini mediche sono pochi e ognuno contiene pochi esempi. Nel caso del canale alveolare inferiore, solo un dataset, Maxillo, ad oggi è disponibile e contiene 91 esempi con una etichettatura densa mentre 200 con solo un'etichettatura sparsa (mentre nei dataset non medici, solitamente ha un numero di esempio dell'ordine di  $10^5$ ). Questo problema è dato dal fatto che per annotare immagini mediche è necessario che un medico esperto le analizzi e le etichetti a mano, cosa che richiede molto tempo ed è anche molto costosa. Un'altra caratteristica delle immagini mediche è che la zona da etichettare è solitamente molto piccola rispetto al volume completo, e questo rende più difficile l'apprendimento della rete.

Il lavoro di questa tesi è stato inizialmente quello di fare un refactoring del codice precedentemente scritto, in modo da ottimizzare alcuni processi, come la lettura e il caricamento dei dati, migliorare l'usabilità e la mantenibilità e poter effettuare i test necessari in modo molto più efficace. Successivamente si è studiata l'efficacia di diverse tecniche proposte in letteratura, con lo scopo di migliorare lo stato dell'arte. Durante la tesi, ho potuto anche contribuire ad una libreria open source, TorchIO, estremamente utilizzata per caricare e processare immagini mediche insieme alle reti neurali profonde, aggiungendo una nuova funzionalità, inizialmente proposta da altri, che si è dimostrata molto efficace anche nei nostri esperimenti.

## *Acknowledgements*

First and foremost, I would like to express my gratitude to my supervisors, Prof. Federico Bolelli and Prof. Costantino Grana, for their guidance, support, and encouragement throughout my work. I would also like to thank them for introducing me to the world of academic research by bringing me with them to a conference, and for inspiring me to continue my studies by enrolling in a Ph.D. program. Thanks goes also to my family and my friends for their unwavering support because, without them, I would not be the person I am today.

# Contents

<b>Abstract in English</b>	<b>i</b>
<b>Abstract in Italian</b>	<b>ii</b>
<b>Summary in Italian</b>	<b>iii</b>
<b>Acknowledgements</b>	<b>1</b>
<b>Contents</b>	<b>2</b>
<b>List of Figures</b>	<b>5</b>
<b>List of Tables</b>	<b>6</b>
<b>List of Listings</b>	<b>7</b>
<b>1 Segmentation of the Inferior Alveolar Canal: an overview</b>	<b>8</b>
1.1 Introduction . . . . .	8
1.2 Inferior Alveolar Canal . . . . .	9
1.3 Cone Beam Computed Tomography . . . . .	9
1.4 DICOM file format . . . . .	10
1.5 Image Segmentation . . . . .	10
<b>2 Segmentation Neural Networks</b>	<b>12</b>
2.1 Supervised Learning . . . . .	12
2.1.1 Backbone networks . . . . .	12
2.1.1.1 U-Net and V-Net . . . . .	12
2.1.1.2 Recurrent Neural Networks . . . . .	13
2.1.1.3 Pseudo-3D Networks . . . . .	13
2.1.1.4 Generative Adversarial Networks . . . . .	13
2.1.2 Network Function Block . . . . .	14

2.1.2.1	Dense connection . . . . .	14
2.1.2.2	Inception block . . . . .	14
2.1.2.3	Depth separability . . . . .	15
2.1.2.4	Attention . . . . .	16
2.1.3	Loss functions . . . . .	17
2.1.3.1	Cross Entropy . . . . .	17
2.1.3.2	Dice Loss . . . . .	17
2.1.3.3	Generalized Dice Loss . . . . .	18
2.1.3.4	Boundary Loss . . . . .	18
2.2	Weakly Supervised and Unsupervised Segmentation . . . . .	19
2.2.1	Data Augmentation . . . . .	19
2.2.1.1	Traditional methods . . . . .	19
2.2.1.2	Conditional Generative Adversarial Networks . . . . .	20
2.2.2	Sparse Labels . . . . .	20
2.2.3	Transfer Learning . . . . .	20
2.3	Current direction of research . . . . .	21
2.3.1	Network Architecture Search . . . . .	21
2.3.2	Graph Convolutional Neural Network . . . . .	22
2.3.3	Interpretable Shape Attentive Neural Network . . . . .	22
2.3.4	Vision Transformer . . . . .	23
<b>3</b>	<b>The Maxillo Dataset</b>	<b>24</b>
3.1	Introduction . . . . .	24
3.2	Dataset . . . . .	25
3.2.1	2D sparse annotations . . . . .	26
3.2.2	3D dense annotations . . . . .	27
3.2.3	Pre-processing with $\alpha$ -shape . . . . .	29
<b>4</b>	<b>Code Refactoring</b>	<b>32</b>
4.1	Introduction . . . . .	32
4.2	Reference Work . . . . .	32
4.2.1	Positional PadUNet3D . . . . .	33
4.2.2	Deep Label Propagation . . . . .	34
4.3	Refactoring . . . . .	34
4.3.1	Data Loading . . . . .	34
4.3.2	Data Augmentation . . . . .	35
4.3.3	Config and command line arguments . . . . .	36
4.3.4	Interfaces . . . . .	36
4.3.5	Deploying and Running . . . . .	36
<b>5</b>	<b>Trying to improve the State of the Art</b>	<b>37</b>
5.1	Boundary Loss . . . . .	37
5.1.1	Formulation . . . . .	38

5.1.2	Combining with other loss functions . . . . .	38
5.2	PosDeepLab v3+ . . . . .	39
5.3	PosSegNet . . . . .	40
5.4	SwinUNETR3D . . . . .	40
5.4.1	Transformer Architecture . . . . .	41
5.4.2	Vision Transformer . . . . .	42
5.4.3	Swin Transformer . . . . .	42
5.4.4	Final Architecture and pre-training . . . . .	43
5.5	Hann window function . . . . .	46
5.5.1	Hann window function in 1D . . . . .	47
5.5.2	Hann window function in 3D . . . . .	47
5.5.3	Implementation . . . . .	47
5.6	Performance improvements . . . . .	50
5.7	Results . . . . .	50
<b>6</b>	<b>Conclusions and future work</b>	<b>51</b>
6.1	Conclusion . . . . .	51
6.2	Recommendation for Future Work . . . . .	51
<b>Bibliography</b>		<b>53</b>

# List of Figures

1.1	Example of a multiclass semantic segmentation, different colors represent different classes . . . . .	11
3.1	2D and 3D annotations of the same patient. . . . .	25
3.2	Axial slice. . . . .	26
3.3	Panoramic view and its annotation. . . . .	27
3.4	Cross-Sectional Lines. . . . .	28
3.5	Cross-Sectional Lines. . . . .	29
3.6	The annotation tool outputs a dense and jagged point set (a), which shape is given by the concave $\alpha$ -shape (b). Finally, the obtained polygonal mesh undergoes voxelization, resulting in a binary raster volume (c) that is used as ground truth for the training process. . . . .	30
3.7	$\alpha$ -shape construction process for the point set of 3.7a, with $\alpha = -2.5$ . First the Delaunay triangulation is built 3.7b, then only triangles whose circumradius is at most $-\frac{1}{\alpha}$ are kept, which form a subcomplex called $\alpha$ -complex 3.7c. Finally, the border of the $\alpha$ -complex is the $\alpha$ -shape 3.7d. . . . .	30
4.1	SubjectsDataset class and its relationships. . . . .	35
5.1	DeepLab v3+ architecture . . . . .	39
5.2	SegNet architecture . . . . .	40
5.3	Transformer architecture . . . . .	41
5.4	Vision Transformer architecture . . . . .	42
5.5	Swin Transformer components . . . . .	43
5.6	SwinUNETR architecture . . . . .	44
5.7	Pre-training phase . . . . .	45
5.8	Different Hann window functions in 2D based on the position of the extracted patch. . . . .	48

## **List of Tables**

# List of Listings

5.1	Python code to generate a $N$ -dim Hann window . . . . .	48
5.2	Code to apply Hann window to a batch of patches given their locations . . . . .	49
5.3	Code to compute the final segmentation . . . . .	49

# **Chapter 1**

## **Segmentation of the Inferior Alveolar Canal: an overview**

### **1.1 Introduction**

Dental implant placement within the jawbone is a routine surgical procedure that can become complicated due to the presence of the Inferior Alveolar Nerve (IAN) nearby. The nerve, in particular, is frequently in close proximity to the roots of molars, and its position must thus be meticulously detailed prior to surgical removal. Avoiding contact with the IAN is a primary concern during these operations, thus its segmentation is crucial in surgical planning. Today the standard de-facto is to take a CBCT scan of the jawbone and a 2D panoramic view is extracted. This view allows medical experts to depict the IANs position with line. We refer to this type of annotation as *sparse* or *2D* annotation. A 3D annotation of the IAC is often avoided as it would require a huge amount of time, but this type of segmentation would offer a much more precise knowledge of the position of the IAN and IAC and could allow dentists to plan a more detailed surgical approach. For this reason, a lot of research about automatic segmentation of the IAC has been carried out and is still active today.

In this chapter, we first describe in detail the role of the IAN and the IAC, what a CBCT is and the definitions and characteristics of different types of segmentations, to give a brief introduction on which are the main components of the final work. In the following chapter, we will look at the main components used to perform image segmentation in the medical

field, until today state of the art. Next in chapter 3, we will detail the dataset that has been used, by describing how it has been created, preprocessed, and some other thoughts. In chapter 4, the network I've used as starting point and the benefits obtained by refactoring the code. Finally, in chapter 5, we will discuss the different approaches taken to try to improve the current state of the art, the results obtained and some of the possible future works.

## 1.2 Inferior Alveolar Canal

The Inferior Alveolar Canal (IAC) is a small passageway shaped as a tube that runs through the lower jawbone. It houses the Inferior Alveolar Nerve (IAN), which is responsible for transmitting sensory information from the teeth, gums, and lips to the brain. It also provides motor innervation to the muscles of mastication (i.e. the muscles responsible for chewing). Dentists need to be able to accurately locate the IAC before performing certain surgical operations, such as tooth extractions or placement of dental implants. This is because the IAC is located very close to the roots of the teeth, and damage to the IAC during surgery can result in permanent nerve damage which would cause numbness, tingling, and pain in the affected area. In severe cases, it can also lead to muscle weakness and paralysis.

## 1.3 Cone Beam Computed Tomography

Cone beam computed tomography (CBCT) is a medical imaging technique consisting of X-ray computed tomography where rays are divergent, forming a cone. This type of computed tomography is well suited for imaging the craniofacial area as it provides clear images of highly contrasted structures, very helpful to evaluate bones. It has become common in dentistry such as oral surgery, endodontics, and orthodontics. The main reasons and advantages of CBCT concerning other CTs are:

1. **X-ray beam limitation:** reducing the size of the irradiated area by collimating the primary x-ray beam to the area of interest minimizes the radiation dose. Most CBCT units can be adjusted to scan small regions for a specific diagnostic task. They are also able to scan the whole craniofacial structure if needed.

2. **Image accuracy:** We created a novel, large, and publicly available maxillo-facial CBCT (Cone Beam Computed Tomography) dataset, with 2D and 3D manual annotations, provided by expert clinicians. All CBCT units provide voxel resolutions that are isotropic (i.e. equals in all the 3 dimensions) while in conventional CT, voxels are anisotropic (i.e. rectangular cubes).
3. **Rapid scan time:** CBCT acquires all the basis images in a single rotation, thus scan time goes from 10s to 70s. Although faster scanning time usually means fewer basis images from which to reconstruct the volumetric dataset, motion artifacts due to subject movement are reduced.

These advantages come with some drawbacks: Hounsfield units (HU) is the metric used to determine the radiodensity of tissue analyzed. In the Hounsfield scale, numbers go from values of  $-1000$  for air to values of  $1600$  for dense bones. In CBCT scans, the radiodensity is inaccurate because different areas in the scan appear with different greyscale values depending on their relative positions in the organ being scanned, despite possessing identical densities, because the image value of a voxel of an organ depends on the position in the image volume. HU measured from the same anatomical area with both CBCT and medical-grade CT scanners are not identical and are thus unreliable for determination of site-specific, radiographically-identified bone density for purposes such as the placement of dental implants, as there is "no good data to relate the CBCT HU values to bone quality" [1].

The images resulting from CBCT scans are usually exported as DICOM (Digital Imaging and Communications in Medicine) which is the standard used worldwide to store, exchange, and transmit medical images.

## 1.4 DICOM file format

TODO?

## 1.5 Image Segmentation

Image segmentation is a well-known topic in computer and image processing with a wide range of applications, such as medical imaging, robotics, video surveillance, etc. It involves partitioning images into one or more objects and can also include classifying these objects.

Many traditional algorithms have been developed in the literature but, in the most recent years, they have all been dominated by deep neural networks. Since 2015 a huge amount of different types of networks that aim to perform image segmentation have been proposed for each field where it's needed. Before presenting how nowadays segmentation is performed, we must state which are the different types of segmentation that have been classified:

- **Semantic segmentation:** Semantic Segmentation performs a pixel-by-pixel classification with a predefined set of object categories for all the pixels of the images. In practice, given a RGB image ( $\text{height} \times \text{width} \times 3$ ) we output a segmentation map of size ( $\text{height} \times \text{width} \times \text{classes}$ ) where each value corresponds to which class the same pixel in the original images belong.
- **Instance segmentation:** One possible issue of semantic segmentation is that it doesn't allow distinguishing two or more objects of the same class when they overlap in the image. Instance segmentation overcomes this problem by outputting a different number of channels based on the number of instances present in the image.
- **Panoptic segmentation:** The latter type of segmentation is called Panoptic segmentation and is the result of the previously presented method joined together. The difference with the instance segmentation is that in this case instances are not allowed to overlap then for a single pixel, a single instance must be assigned.

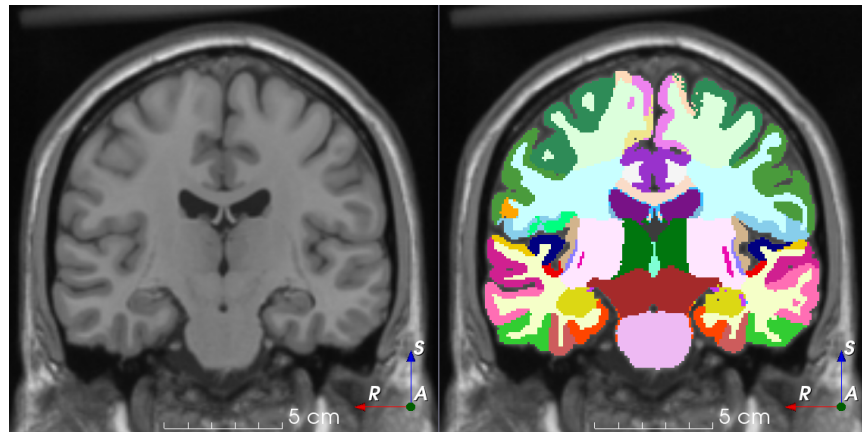


FIGURE 1.1: Example of a multiclass semantic segmentation, different colors represent different classes

# **Chapter 2**

## **Segmentation Neural Networks**

### **2.1 Supervised Learning**

In the medical image segmentation tasks, supervised learning is the most popular method, where the latest improvements mainly include network backbones, network blocks, and the design of novel loss functions.

#### **2.1.1 Backbone networks**

The encoder-decoder structure is the most popular end-to-end architecture, such as fully convolutional networks (FNC) like U-Net, Deeplab, and SegNet. The encoder part aims to extract high-level features from the input image and project them into a latent space. The decoder part instead restores the extracted features from the latent space to the original space size.

##### **2.1.1.1 U-Net and V-Net**

In 2015, Ronneberger *et al.* [2] proposed U-Net which has been widely used for medical image segmentation and many variants have been proposed also in recent years. The structure of U-Net is symmetrical and the main scope is to fuse low-level features, which medical images are usually noisy but show blurred boundaries, with high-level features via skip connections.

U-Net was designed to deal with 2D images but when dealing with medical images, we usually have to handle 3D images. A straightforward solution was to extract 2D slices from the original image and feed them to the network and stack the outputs to obtain the final 3D output. The main drawback of this approach is that we lost the spatial information among the slices as they are treated as independent images. Motivated by this idea, Çiçek *et al.* [3] proposed a solution to this problem by using 3D convolutions inside U-Net. This network, named 3D U-Net, includes only three down-sampling steps because of the high computational cost of 3D Convolutions, leading to less effective extraction of deep-layer image features. Milletari *et al.* [4] proposed a similar architecture, named V-Net, which employs more skip connections than U-Net to design a deeper network. Some Recurrent Neural Network mixed with U-Net has also been proposed to model the time dependence of image sequences.

### 2.1.1.2 Recurrent Neural Networks

Gao *et al.* [5] joined LSTM and CNN to model the temporal relationships between different brain MRI slices to improve segmentation accuracy. RNN can capture local and global spatial features of images by considering the context information relationship. However, in medical image segmentation, the capture of complete and valid temporal information requires good medical image quality (e.g. smaller slice thickness and pixel spacing). Therefore, the design of RNN is uncommon for improving the performance of medical image segmentation.

### 2.1.1.3 Pseudo-3D Networks

As stated before, most medical images are 3D images but using 3D convolution requires a lot of computational resources. Therefore some pseudo-3D segmentation methods have been proposed. For example, Vu *et al.* [6] applied the overlay of adjacent slices as input to the central slice prediction and then fed the obtained 2D feature map into a standard 2D network.

### 2.1.1.4 Generative Adversarial Networks

Another type of networks that has been exploited in medical image segmentation are Generative Adversarial Networks (GANs) [7], mostly used in data augmentation by generating new samples. Pollastri *et al.* [8] remodeled two different well-known GANs, Deep Convolutional

GAN, and a Laplacian GAN, to generate both skin lesion images and their segmentation masks, making the augmentation process extremely straightforward. In addition, the incorporation of prior knowledge about organ shape and position may be crucial for improving the medical image segmentation effect, where images are corrupted and thus contain artifacts due to limitations of imaging techniques. However, there are few works about how to incorporate prior knowledge into CNN models. As one of the earliest studies in this field, Oktay *et al.* [9] proposed a novel and general method to combine a priori knowledge of shape and label structure into the anatomically constrained neural networks (ACNN) for medical image analysis tasks. In this way, the neural network training process can be constrained and guided to make more anatomical and meaningful predictions, especially in cases where input image data is not sufficiently informative or consistent enough (e.g., missing object boundaries).

After proposing U-Net in [2], the encoder-decoder structure became the most popular structure in medical image segmentation. The design of the network backbone focuses on more efficient feature extraction in the encoder and feature recovery and fusion in the decoder to improve segmentation accuracy.

## 2.1.2 Network Function Block

### 2.1.2.1 Dense connection

Dense connection is the most popular network block in medical image segmentation, used to construct a kind of special convolution neural network. The input of each layer comes from the output of all previous layers in the process of forwarding transmission. Inspired by this design, Guan *et al.* [10] proposed an improved U-Net by replacing each sub-block of the network with a form of dense connection. Although the dense connection helps obtain richer image features, it often reduces the robustness of feature representation to a certain extent and increases the number of parameters.

### 2.1.2.2 Inception block

For CNNs, deep networks often give better performances than shallow ones, but they encounter some new problems such as vanishing gradient, high memory usage, and slow convergence. The inception structure used in GoogleNet [11, 12] overcomes these problems,

and for this reason, it has been also used over medical images. Gu *et al.* [10] proposed CE-Net by introducing the inception structure and atrous convolution to each parallel structure to extract features on a wide reception field. Such complex structure however leads to a difficult model modification.

### 2.1.2.3 Depth separability

To reduce the computational cost of 3D convolutions and their memory usage, Howard *et al.* [13] proposed MobileNet to decompose vanilla convolutions into depthwise separable convolution and pointwise convolution. A standard convolution layer takes as input a 3D volume  $X$  of shape  $(l_x, w_x, h_x, c_x)$  and outputs a 3D volume  $Y$  of shape  $(l_y, w_y, h_y, c_y)$ , while the kernel will be of shape  $(k, k, k, c_x, c_y)$ , where  $k$  is the kernel size. The output will be computed as:

$$Y_{l,w,h,n} = \sum_{i,j,k,m} K_{i,j,k,m,n} \cdot X_{l+i-1, w+j-1, h+k-1, m} \quad (2.1)$$

where  $x, y, z$  and  $i, j, k$  denotes voxel's spatial position and  $m$  denotes the input channels while  $n$  denotes the output channels. And the computation cost would be:

$$\mathcal{O}(l_x \cdot w_x \cdot h_x \cdot k^3 \cdot c_x \cdot c_y) \quad (2.2)$$

For the depthwise convolution, we decompose the procedure explained above in two steps by using two different filters. The first step is to apply a filter for each individual channel, and the second step is to apply a  $1 \times 1 \times 1 \times c$  filter to combine the results. ReLU and batch normalization are applied after both steps. The output for a 3D depthwise convolution is:

$$\hat{Y}_{x,y,z,m} = \sum_{i,j,k,m} \hat{K}_{i,j,k,m} \cdot X_{x+i-1, y+j-1, z+k-1, m} \quad (2.3)$$

where  $x, y, z$  and  $i, j, k$  again denotes the spatial position of a voxel.  $\hat{K}$  will be a depthwise convolution kernel of size  $k \times k \times k \times c_x$  and the  $m$ -th filter in  $\hat{K}$  will be applied to the  $m$ -th channel in  $X$ , while the output of the  $m$ -th filter becomes the  $m$ -th layer in  $\hat{Y}$ . Next we have to combine each channel by using the  $1 \times 1 \times 1 \times c$  filter at every position of the feature map, essentially carrying out a linear combinations of layers of all depths, fusing the splitted channels back together.

The total cost will be:

$$\mathcal{O}(k^3 \cdot c_x \cdot l_x \cdot w_x \cdot h_x + c_x \cdot c_y \cdot l_x \cdot w_x \cdot h_x) \quad (2.4)$$

By dividing 2.4 by 2.2, we can compute how much more efficient depthwise separable convolution is compared to vanilla 3D convolution:

$$\frac{\mathcal{O}(k^3 \cdot c_x \cdot l_x \cdot w_x \cdot h_x + c_x \cdot c_y \cdot l_x \cdot w_x \cdot h_x)}{\mathcal{O}(l_x \cdot w_x \cdot h_x \cdot k^3 \cdot c_x \cdot c_y)} = \frac{1}{c_y} + \frac{1}{k^3} \quad (2.5)$$

Usually, the filter has a size of  $3 \times 3 \times 3$ , and the number of channels can vary from 64 to 512. Therefore, separable convolutions are from  $\frac{1}{\frac{1}{27} + \frac{1}{64}} = 18.99$  to  $\frac{1}{\frac{1}{27} + \frac{1}{512}} = 25.65$  times more efficient than standard convolutions.

#### 2.1.2.4 Attention

Attention block can selectively change input or assigns different weights to input variables according to different importance.

*Spatial Attention* block aims to calculate the feature importance of each pixel in the space domain and extract the key information of an image. Oktay *et al.* [14] proposed attention U-Net, where attention blocks were used to change the output of the encoder before fusing features from the encoder and the corresponding decoder. The attention block outputs a gating signal to control the feature importance of pixels at different spatial positions.

Another type of attention block is the *Channel attention*, which utilizes learned global information to emphasize selectively useful features and suppress useless features. Hu *et al.* [15] proposed SE-Net introducing the channel attention to the field of image analysis and winning the ImageNet Challenge in 2017.

Spatial and channel attention mechanisms are the two most popular strategies for improving feature representation. However, spatial attention ignores the difference between different channel information and treats each channel equally. On the contrary, channel attention pools global information directly while ignoring local information in each channel, which is a relatively rough operation. Therefore, combining the advantages of two attention mechanisms, researchers have designed many models based on a *mixed domain attention block*.

### 2.1.3 Loss functions

In addition to improved segmentation speed and accuracy by designing the network backbone and the function block, designing new loss functions also resulted in improvements in subsequent inference-time segmentation accuracy. Therefore, a great deal of work has been reported on the design of suitable loss functions for medical image segmentation tasks.

#### 2.1.3.1 Cross Entropy

The cross-entropy loss has been the most popular loss function. It compares pixel-wisely the predicted category vector with the real segmentation result vector and is defined as:

$$L_{CE} = - \sum_{i=1}^N \sum_{j=1}^C y_{ij} \log \hat{y}_{ij}$$

where  $y_{ij}$  is the real segmentation result vector,  $\hat{y}_{ij}$  is the predicted segmentation result vector,  $n$  is the number of pixels in the image, and  $C$  is the number of categories. The cross-entropy loss is easy to implement and has been widely used in medical image segmentation tasks. However, it is not suitable for segmentation tasks with imbalanced data, because it does not consider the class imbalance problem. Therefore, a *weighted cross entropy loss* [16] and *balanced cross entropy* have been proposed to solve this problem, where a  $\beta$  hyper-parameters are added to the loss function to adjust the weight of each class.

#### 2.1.3.2 Dice Loss

The Dice coefficient is a popular metric for the evaluation of medical image segmentation tasks. This metric is the measure of overlap between a segmentation result and its corresponding ground truth:

$$DSC = \frac{2 \times |A \cap B|}{|A| + |B|}$$

where  $A$  and  $B$  are the segmentation result and the ground truth, respectively. The *Dice Loss*, for the first time proposed in the V-Net paper [4], is formulated as a continuous relaxation of the Dice coefficient:

$$L_{DSC} = 1 - \frac{2 \times y \times \hat{y} + 1}{y + \hat{y} + 1}$$

Here 1 is added to the denominator to avoid the division by zero in the edge case when both  $y$  and  $\hat{y}$  are zero. The Dice loss is a good choice even for uneven samples, however, it easily influences the backpropagation and leads to a training difficulty.

### 2.1.3.3 Generalized Dice Loss

Although Dice Loss can solve the problem of class imbalance to a certain extent, it does not work for serious class imbalance. To solve this problem, researchers have proposed a *Generalized Dice Loss* [17] that can be used for both binary and multi-class segmentation tasks. The generalized Dice loss is defined as:

$$L_{GDSC} = 1 - \frac{1}{m} \frac{2 \sum_{j=1}^m \omega_j \sum_{i=1}^n y_{ij} \hat{y}_{ij}}{\sum_{j=1}^m \omega_j \sum_{i=1}^n (y_{ij} + \hat{y}_{ij})}$$

where the weight  $\omega_j$  is used to adjust the weight of each class, and  $\omega_j = 1/(\sum_{i=1}^n p_{ij})^2$ .

### 2.1.3.4 Boundary Loss

Another approach that solves the problem of class imbalance has been proposed by Ker-vadec *et al.* [18] for the task of brain lesion segmentation. They proposed a Boundary Loss which aims to minimize the distance between segmented boundaries and labeled boundaries. Results show that the combination of the Dice loss and the boundary loss is superior to the single ones. The composite loss is defined as:

$$L = \alpha L_{DSC} + (1 - \alpha) L_B$$

where the Boundary Loss  $L_B$  for a binary segmentation is defined as:

$$L_B = \sum \phi(y) \times \hat{y}$$

where  $\phi(y)$  is the signed distance function applied to the real segmentation  $y$ .

For medical image segmentation, the improvement of loss mainly focuses on the problem of segmentation of small objects in a large background (the problem of class imbalance). Chen *et al.* [18] proposed a new loss function by applying traditional active contour energy minimization to convolutional neural networks, Li *et al.* [19] proposed a new regularization term to improve the cross-entropy loss function, and Karimi *et al.* [20] proposed a loss function

based on Hausdorff distance (HD). Besides, there is still a lot of work trying to deal with this problem by adding penalties to loss functions or changing the optimization strategy according to specific tasks.

In many medical image segmentation tasks, there are often only one or two targets in an image, and the pixel ratio of targets is sometimes small, which makes network training difficult. Therefore, to improve network training and segmentation accuracy, it is easier to focus on smaller targets by changing loss functions than to change the network structure. However, the design of loss functions is highly task-specific, so we need to analyze carefully task requirements, and then design reasonable and available loss functions.

## 2.2 Weakly Supervised and Unsupervised Segmentation

Although convolutional neural networks show goods performances for medical image segmentation, results seriously depend on high-quality labels. It is rare to build many datasets with many high-quality labels, especially in the field of medical image analysis, since data acquisition and labeling often incur high costs. Therefore, a lot of studies on incomplete or imperfect datasets are reported. Unsupervised learning is a very important approach that improves the performance of medical image segmentation. In this section, we will introduce weakly supervised learning, a method that makes use of unsupervised learning for unlabelled data in combination with supervised learning with labeled data.

### 2.2.1 Data Augmentation

Performing data augmentation is mandatory in absence of a largely labeled dataset, and is still considered good practice even when we have enough data. However, new data generated with this method produce images that are highly correlated with the original images.

#### 2.2.1.1 Traditional methods

With traditional methods, we refer to all the computer vision techniques such as adding/removing noise, changing brightness, saturation, contrast, colors, and changing the image layout with rotations, distortion, scaling, etc. These techniques are still very used today, usually combining them together with random parameters. Some of these algorithms may require a non-negligible computational cost thus usually performed before the training procedure.

### 2.2.1.2 Conditional Generative Adversarial Networks

As already described in Section 2.1.1.4, GAN and its variants have been widely used for data augmentation. In particular, cGANs are often used in combination with standard GANs to generate labels relative to a given synthetic image.

### 2.2.2 Sparse Labels

Cipriano *et al.* [21] recently proposed a pre-training approach based on sparse labels. This type of labels are way easier to obtain but is not as accurate as the real dense labels. They fed these labels to the network together with the input image for a given number of steps, then used the learned parameters to produce dense labels for a set of images that had only the sparse labels. The authors showed that this approach can be used to improve the performance of the final network.

### 2.2.3 Transfer Learning

Pre-trained model parameters are often used to initialize a new model, transfer learning can achieve fast training for data with limited labels. The most popular approach is to use a model pretrained on ImageNet before performing the training on the medical data. Experiments demonstrated that this approach is useful as it improves the accuracy of segmentations. However, domain adaptation may be a problem when applying models trained over natural images to medical image analysis tasks. Moreover, these methods are hardly applicable to 3D medical image analysis because such pre-trained models rely on 2D datasets.

Tang *et al.* [22] recently proposed an unsupervised approach to pre-train a given model by relying only on unannotated medical images of the same domain of the main tasks. In practice, the network is trained to perform a variety of tasks such as image reconstruction, classification of the rotation applied to the original image, etc. which can be performed in an unsupervised manner. Later, these tasks heads of the network are detached and the training on the main task is performed. Such pretraining aims to train the network to learn how to extract high-level features from a specific type of medical images, such as CT or MRI.

## 2.3 Current direction of research

Until now we described the most popular network structures and loss functions for medical image segmentation tasks that were proposed and used up to date. Since the rise in the popularity of vision transformers and graph neural networks, some novelty architectures are being proposed in medical imaging. Results obtained are still not as good as those obtained with traditional architectures, aside from some really specific tasks or datasets, but they are still interesting and promising.

### 2.3.1 Network Architecture Search

The design process of network architecture is a very time-consuming task, and it is often difficult to find the best architecture for a given task. Therefore, many researchers have proposed methods to automate the design of network architectures. Such methods, named NAS (Network Architecture Search) [23], focus on the *search space*, *search strategy*, and *performance estimation*. The search space is a candidate collection of network structures to be searched and it is divided into a global search space that represents the search for the entire network structure, and a cell-based search space that searches only a few small structures that are assembled into a complete large network by the ways of stacking and stitching. The search strategy aims to find the optimal network structure as fast as possible in search spaces. Popular search strategies are often grouped into three categories, reinforcement-based learning, evolutionary algorithms, and gradients. The performance estimation strategy is the process of assessing how well the network structure performs on target datasets. For NAS techniques, researchers pay more attention to the improvement of search strategies since search space and performance estimation methods are usually rarely changed.

Isensee *et al.* [24] argued that too much manual adjustment on network structure could lead to over-fitting for a given dataset, and therefore proposed a medical image segmentation framework no-newUNet (nnU-Net) that adapts itself to any new dataset. The nnUNet automatically adjusts all hyperparameters according to the properties of the given dataset without manual intervention. Therefore, the nnU-Net only relies on vanilla 2D UNet, 3D UNet, UNet cascade, and a robust training scheme. It focuses on the stage of pre-processing (resampling and normalization), training (loss, optimizer settings, data augmentation), inference (patch-based strategies, test-time-augmentations integration, model integration, etc.), and post-processing (e.g., enhanced single pass domain). In practical applications, the improvements in network structure design usually depend on experiences without adequate

interpretability theory support. Moreover, more complex network models indicate a higher risk of over-fitting.

### 2.3.2 Graph Convolutional Neural Network

Graph Convolutional Neural Network (GCN) is a type of neural network that utilizes graph structure to process data. In practice, the Euclidean space of the image can be converted into graphs that can be modeled using GCN.

Gao *et al.* [25] designed a new graph pooling (gPool) and graph unpooling (gUnpool) operation based on GCN and proposed an encoder-decoder model namely graph U-Net. The graph U-Net achieves better performance than popular UNets by adding a small number of parameters. In contrast to traditional convolutional neural networks where deeper is better, the performance of the graph U-Net cannot be improved by increasing the depth of networks when the value of depth exceeds 4. However, the graph U-Net shows a stronger capability of feature encoding than popular U-Nets when the value of depth is smaller or equivalent to 4.

Yang *et al.* [26] proposed the end-to-end conditional partial residual plot convolutional network CPR-GCN for automatic anatomical marking of coronary arteries. Authors showed that the GCN-based approach provided better performance and stronger robustness than traditional and recent depth learning-based approaches. Results from these GCNs in medical image segmentations are promising, as the graph structure has high data representation efficiency and a strong capability of feature encoding.

### 2.3.3 Interpretable Shape Attentive Neural Network

Currently, many deep learning algorithms tend to make judgments by using "memorized" models that approximately fit input data. As a result, these algorithms cannot be explained sufficiently and give convincing evidence for each specific prediction. Therefore, the study of the interpretability of deep neural networks is a hot topic at present Sun *et al.* [27] proposed the SAU-Net which focuses on the interpretability and robustness of models. The proposed architecture attempts to address the problem of poor edge segmentation accuracy in medical images by using a secondary shape stream. Especially, the shape stream and the regular texture stream can capture rich shape-dependent information in parallel. Furthermore, both spatial and channel attention mechanisms are used for the decoder to explain the learning

capability of models at each resolution of U-Net. Finally, by extracting the learned shape and spatial attention maps, we can interpret the highly activated regions of each decoder block. The learned shape maps can be used to infer the correct shapes of interesting categories learned by the model. The SAU-Net can learn robust shape features of objects via the gated shape stream and is also more interpretable than previous works via built-in saliency maps using attention.

### 2.3.4 Vision Transformer

Recently, transformer-based architectures have become very popular and replaced the convolutional operator and use self-attention modules to compose entire encoderdecoder structures that can encode long-range dependencies. It has been a great success in the field of natural language processing. Dosovitskiy *et al.* [28] proposed Vision Transformer (ViT) that can classify images directly using the Transformer. Recently, a large number of researchers have applied the transformer to medical image segmentation. CNNs have a comparative advantage in extracting the underlying features. These low-level features form the key points, lines, and some basic image structures at the patch level. However, when we detect these basic visual elements, the higher-level visual semantic information is often more concerned with how these elements relate to each other to form an object, and how the spatial location of objects relates to each other to form the scene. At present, the transformer is more natural and effective in dealing with the relationships between these elements. However, if all the convolutional operators in computer vision tasks are replaced by Transformer, it may suffer from many problems, such as high computational cost and memory usage. From existing research, the combination of Transformer and CNNs may lead to better results. Recently, Chen *et al.* [29] proposed a U-Net shaped network, where the encoder was made of ViT only while the decoder was fully convolutional.

# **Chapter 3**

## **The Maxillo Dataset**

### **3.1 Introduction**

Nowadays, perfect anatomical annotation accuracy is usually not achieved, in favor of a fast execution time. A sparse annotation (Fig. 3.1a), performed on a 2D image, can be realized in a relatively small amount of time, and has become the de facto standard in radiologic medical centers for dentistry and maxillofacial purposes (a specialty also known as dento-maxillofacial radiology). However, 2D annotations lack a considerable amount of inner information about the bone structure and the IAN position. Surgeons rely on a partial and incomplete idea of nerve positioning, which is generally sufficient for a positive outcome of surgical intervention but does not represent an accurate anatomical representation. Switching to 3D annotations (Fig. 3.1b) solves the issue, but raises the costs in terms of working time: the manual segmentation of a single scan volume, depending on the available software, can take hours. Therefore, although dento-maxillofacial radiology would largely benefit from 3D annotated patients, any manual method currently appears unsuitable for practical applications.

An additional constraint when dealing with the medical branch of deep learning regards the extra consideration for sensitive data, which must always be taken into account. Medical data contain a huge amount of personal information which must be protected through data anonymization. Besides the sensible details about the patient, generally stored in the DICOM format, when it comes to medical imaging, the personal features of one subject can be inherently carried by the images. Therefore, in order to evaluate the correctness of the

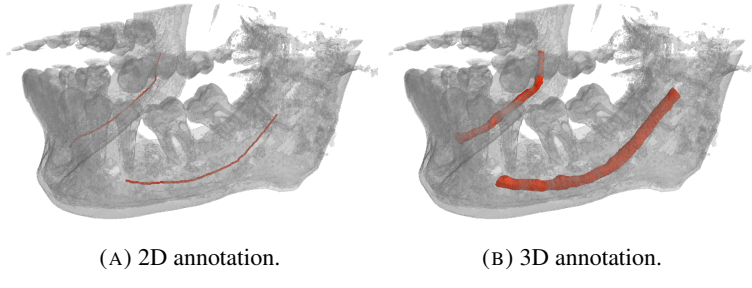


FIGURE 3.1: 2D and 3D annotations of the same patient.

anonymization steps and the security of the information, every medical dataset must undergo evaluation of specific committees. Several bureaucratic steps generally stand before the official release to the scientific community. This circumstance, combined with the laws of individual countries, creates a serious burden for the spread of medical datasets and makes any contribution valuable. For those reasons, deep learning works applied to medical imaging — and in particular, to the maxillofacial field— are often based on private internal datasets. Despite any alleged intention, datasets are rarely released after publication, creating a vast information gap for the research community: researchers are unable to replicate experiments and lack valid benchmarks for their novelties.

## 3.2 Dataset

Cipriano *et al.* [30] have released a public dataset of maxillofacial scans with a sparse and deep labels, which is the first of its kind. The 3D CBCT volumes composing the dataset have been acquired by the Affidea center located in Modena, Italy. Affidea is a leading pan-European healthcare group specialized in the provision of advanced diagnostics, specialist outpatient services, laboratory analyses, physiotherapy and rehabilitation, cancer diagnosis, and treatment. It counts 312 different centers in 15 different countries, with about 11 000 professionals. The dataset counts 347 dental scans obtained by means of Cone Beam Computed Tomography (NewTom/NTVGiMK4, 3 mA, 110 kV, 0.3 mm cubic voxels). Pixel spacing and intra-slice distance are always 0.3 millimeters. Data volumes are already converted to the Hounsfield Unit (HU) and their values range between -1000 and 5264. During the conversion to HU we also took care of the proper processing for the window width and center according to the DICOM format. Volume shapes range from (148, 265, 312) to (178, 423, 463) for the Z, Y and X axes respectively. Every patient was anonymized, hence we were only able to access a few personal details - namely

gender, age, and year of the scan. Specifically, 59% of the patients are female, all the scans were performed between 2019 and 2020, and volumes belong to patients with ages in the range (10 – 100] with the highest frequencies in ranges (20 – 30] and (60 – 70].

### 3.2.1 2D sparse annotations

Technicians involved in the diagnostic exam were also responsible for the original sparse annotation of the mandibular canal. This annotation performed on 2D panoramic views of the jawbone is employed in everyday surgical practice to measure the height and depth of the sites where the implant must be placed, avoiding inferior alveolar nerve injuries. In these labels, the upper bound of the canal is marked along the entire dental arch, providing a useful sparse approximation trace of nerve position. Particularly, the annotation process starts from an axial slice (Fig. 3.2 of the original volume. Upon this slice, a spline is manually drawn to fit the central part of the jawbone.

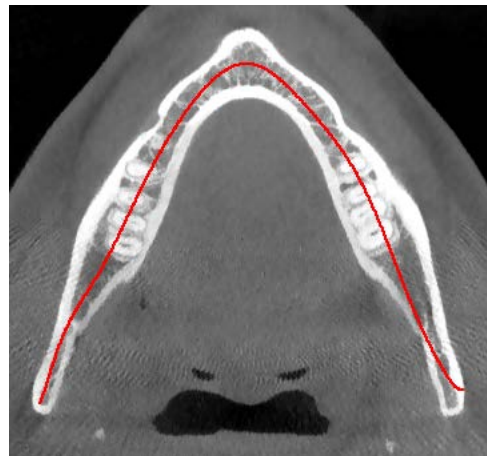
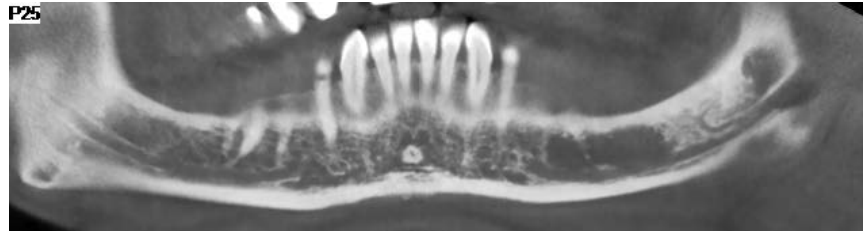


FIGURE 3.2: Axial slice.

This spline, called the panoramic base curve, is then employed for generating the panoramic view (Fig. 3.3a) composed by the voxels of the curved plane identified by the base curve and orthogonal to the axial slice. From this view, the inferior alveolar nerve canal should be clearly identifiable and can be annotated as in Fig. 3.3b.



(A) Panoramic view obtained from the spline drawn on the axial slice.



(B) Panoramic view with the inferior alveolar nerve canal annotated in red.

FIGURE 3.3: Panoramic view and its annotation.

### 3.2.2 3D dense annotations

In order to obtain finely-grained annotations, a team of doctors with years of experience in maxillofacial surgery elaborated 91 volumes to produce dense voxel-level annotations of the canal. The proposed dataset of 347 scans is therefore divided into two partitions: the primary dataset, composed of the 91 volumes for which both dense and sparse annotations are available, and the secondary dataset, only sparsely annotated.

The entire voxel-level annotation procedure has been performed by means of a tool developed by Mercadante *et al.* [31] which allowed to drastically reduce the burden necessary to produce the 3D label. The annotation steps can be summarized as follows:

1. After loading the input data, the arch approximation that better describes the canal course is identified inside one of the axial images and manually adjusted. The output is a one-pixel thick curve crossing the dental arch which is approximated with a polynomial. The result is similar to the one in Fig. 3.2, but this time it is automatically generated and manually adjusted only if needed.
2. Sampling the polynomial, the tool thus generates a Catmull-Rom spline. For each point of the spline, a perpendicular line (lying on the axial plane) is computed (Fig. 3.4). These lines are called Cross-Sectional Lines or CSLs in short. Here, a different resolution of the spline generates more or fewer CSLs. This represents a crucial

step for having a complete annotation of the mandibular canal. Indeed, with a short spline, some regions of the jawbone, especially near the mandibular foramen, would be excluded from the next stages.

3. CSLs are the base of Multi Planar Reformations(MPRs) called Cross-Sectional Views (CSVs). These views are 2D images obtained interpolating the values of the respective baselines (CSL) across the whole volume height. As an example, the blue plane reported in Fig. 3.5 is a Cross-Sectional Plane (CSP) generating a cross-sectional View. CSPs are additionally rotated around the CSLs, to have CSVs orthogonal to the canal slope.
4. For each CSV, a closed Catmull-Rom spline is finally drawn to annotate the position of the IAC (green lines of Fig. 6).
5. The splines are saved as the coordinates of their control points. The final smooth and precise ground-truth volume constituting the dataset is generated from this set of points by means of the  $\alpha$ -shape algorithm [32], which is described in detail in the Section 3.2.3.

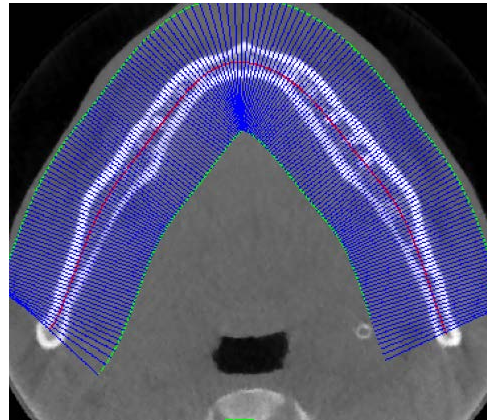


FIGURE 3.4: Cross-Sectional Lines.

Comparing the two procedures, it is possible to see that while sparse annotations are quick and easy to obtain, creating dense labels from 3D volumes is a very tedious and time-consuming process. For this reason, researchers typically have few dense annotations available and preserve them as the test set. Indeed, densely annotated volumes must always be used in tests, to ensure a real medical feedback on model performance.

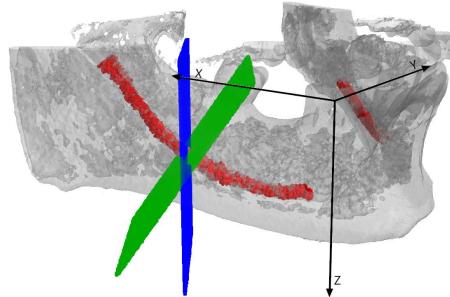


FIGURE 3.5: Cross-Sectional Lines.

### 3.2.3 Pre-processing with $\alpha$ -shape

The hand-drawn ground truth annotations produced with the tool described in the previous section result in a dense and jagged point set; an example is depicted in Fig. 3.6a. Starting from this point set, we reconstruct a smoother polygon mesh in the form of the  $\alpha$ -shape. The  $\alpha$ -shape, defined by Edelsbrunner *et al.* is a generalization of the concept of the convex hull, useful to capture the intuitive notion of the shape of a point set. The definition refers to the 2-dimensional case, but the extension to point sets in  $k$  dimensions is straightforward. The  $\alpha$ -shape is parameterized over  $\alpha \in \mathbb{R}$ , which determines the "crudeness" of the result.

First, a generalized disk of radius  $\frac{1}{\alpha}$ , named  $D_\alpha$ , is defined as:

$$D_\alpha = \begin{cases} \text{The complement of a disc of radius } -\frac{1}{\alpha}, & \text{if } \alpha < 0 \\ \text{A halfplane} & \text{if } \alpha = 0 \\ \text{A disc of radius } \frac{1}{\alpha}, & \text{if } \alpha > 0 \end{cases}$$

Then, given a point set  $S$  and a specific value for  $\alpha$ , the  $\alpha$ -shape graph is constructed in the following way: an edge is created between two points  $p_i$  and  $p_j$  whenever there exists a  $D_\alpha$  containing the entire  $S$ , and which has the property that  $p_i$  and  $p_j$  lie on its boundary. It is straightforward to notice that, when  $\alpha = 0$ , this process constructs the convex hull. Instead, positive or negative values of  $\alpha$  allow building cruder or finer shapes respectively, with the latter possibly including concave angles. Because of the geometrical nature of the alveolar nerve, we are indeed exclusively interested in concave  $\alpha$ -shapes, i.e., with  $\alpha < 0$ . When  $\alpha < 0$ , the  $\alpha$ -shape can be computed starting from the Delaunay triangulation: the set of triangles of the Delaunay triangulation whose circumradius is at most  $\frac{1}{\alpha}$  form a simplicial

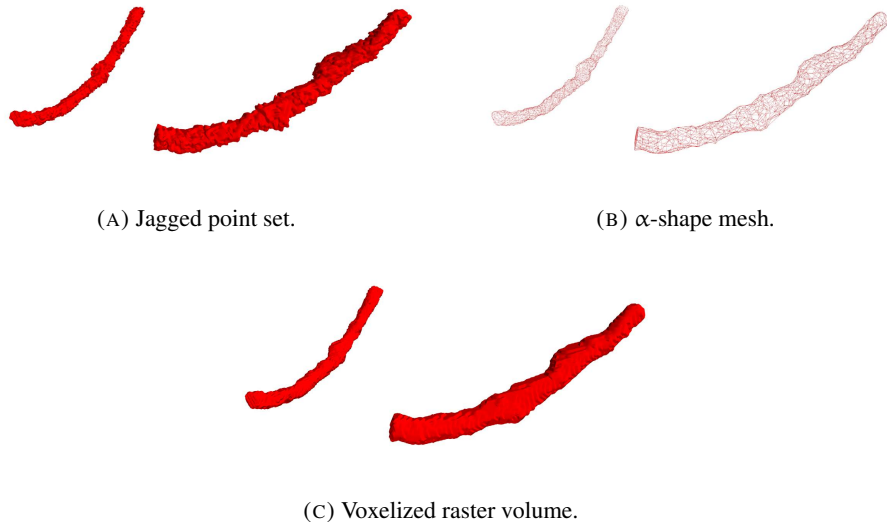


FIGURE 3.6: The annotation tool outputs a dense and jagged point set (a), which shape is given by the concave  $\alpha$ -shape (b). Finally, the obtained polygonal mesh undergoes voxelization, resulting in a binary raster volume (c) that is used as ground truth for the training process.

subcomplex, called  $\alpha$ -complex, and its border coincides with the  $\alpha$ -shape. The process is exemplified in Fig. 3.7.

The generalization of the above notions to 3 dimensions is just a matter of substituting disks and triangles with spheres and tetrahedra. An example of  $\alpha$ -shape constructed from the volumetric annotations of the alveolar nerve is depicted in Fig. 3.6b.

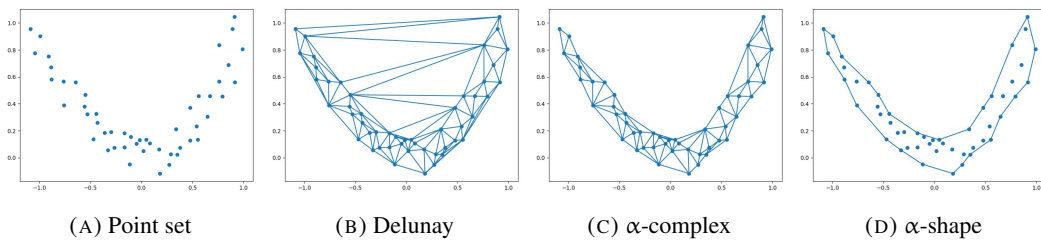


FIGURE 3.7:  $\alpha$ -shape construction process for the point set of 3.7a, with  $\alpha = -2.5$ . First the Delaunay triangulation is built 3.7b, then only triangles whose circumradius is at most  $-\frac{1}{\alpha}$  are kept, which form a subcomplex called  $\alpha$ -complex 3.7c. Finally, the border of the  $\alpha$ -complex is the  $\alpha$ -shape 3.7d.

The  $\alpha$ -shape is a good representation of the annotated volume, but because it is a polygonal mesh, it cannot directly be used as a ground truth segmentation mask for training a neural network. Therefore, the next mandatory step is voxelization, through which the  $\alpha$ -shape is

transformed into a binary raster volume. The voxelization of a polygonal mesh consists of finding which cubes (voxels) of a 3-dimensional grid intersect any triangle composing the mesh: the specific method used to check triangle-cube intersection has been developed by Voorhies. The final result of the ground truth preprocessing is illustrated in Fig. 3.6c.

# **Chapter 4**

## **Code Refactoring**

### **4.1 Introduction**

Cipriano *et al.* spent some effort developing the dataset and a to design a network which was capable to perform the segmentation of the Inferior Alveolar Canal. Together with the novel dataset, they proposed a modified version of U-Net 3D as a backbone for both the label propagation and the IAC segmentation. Both these networks and methods were introduced in the previous chapters and will be explained more in detail in the following sections. As the code was written near the deadline for the submission of the paper, the authors did not have focused on producing a codebase that was optimized for reusability, extensibility, and efficiency. For this reason, my work starts by refactoring the codebase to add these features which improved all my successive experiments.

### **4.2 Reference Work**

The reference work that has been taken as starting point for this work has been made by Cipriano *et al.* in 2022 [21]. The pipeline proposed can be divided into two main steps: the deep label propagation and the IAC segmentation.

### 4.2.1 Positional PadUNet3D

A slightly modified version of 3D U-Net has been proposed as a backbone for both steps. Differently from the original 3D U-Net architecture, every three-dimensional convolution in our CNN applies 2 pixels padding along each dimension. Although this alteration does not cause any variation in terms of performance, it ensures that the output of each convolution has the same size as its input along axis  $x$ ,  $y$ , and  $z$ .

Resolution changes are therefore due uniquely to the three max-pooling layers, each halving the size of the volumes. When using the aforementioned input size, the encoder output is composed of 512 feature maps of size  $10 \times 10 \times 10$ . Inside the decoder, on the other hand, resolution changes are caused by transposed convolutions, with dimensions  $2 \times 2 \times 2$  for both the kernel and stride to double the size of the feature maps. This adjustment ensures resolution symmetry between features in the decoder and corresponding maps in the encoder, thus allowing them to be simply concatenated with skip connections. Moreover, the output of the model naturally has the same dimensions as the input. The final output is a single channel volume, to which we apply a Sigmoid activation function and a threshold at 0.5 to obtain the final binary prediction mask.

The segmentation architecture is further enriched with a positional embedding. Since our sub-volumes are extracted from the original scan following a fixed grid, we exploit positional information derived from the location of the top-left and bottom-right corners of the sub-volume. Specifically, these global coordinates are fed to a linear layer which yields a single feature map of dimensions  $10 \times 10 \times 10$ . This positional embedding gets concatenated to the output of the encoder, and then fed to the decoder. Exploiting positional information ensures two extremely important benefits:

- During training, the CNN is fed with implicit information about areas close to the edges of the scan, where the IAN is very unlikely to be present. This piece of knowledge greatly reduces the number of false positives during inference. As a matter of fact, no postprocessing method is required to refine the output of the proposed CNN
- Information about cut positions helps the network to better shape the output: sub-volumes located close to the mental foramen generally present a much thinner canal than those located in the mandibular foramen. This technique could indeed be employed for several classes of medical data, as anatomical structures can substantially vary according to their location.

### 4.2.2 Deep Label Propagation

The presence of a new 3D voxel-level annotated dataset paves the way to a new frontier for label propagation: we can indeed employ 3D annotations to supervise a deep label propagation neural network, trained to expand sparse labels into dense ones, and produce high-quality synthetic ground truths for the segmentation task. We christen this new label propagation approach Deep Label Expansion, or Deep Expansion in short. The deep expansion model is based on the proposed segmentation network, Positional PadUNet. The main difference regards the input layer, which is changed in order to accept a concatenation of both the raw volume data and the sparse annotations, rendered as a binary channel. Thus, the network input has a shape of  $2 \times 80 \times 80 \times 80$ . Same as Positional PadUNet, a positional embedding is concatenated to the encoder output. By means of this model, we generate a synthetic dataset which will be employed to pre-train our final segmentation CNN. Once again, the positional embedding supplies important information about the location of the cut, which is closely related to the diameter of the expanded labeled canal.

## 4.3 Refactoring

The code was divided into two main repositories, one for the label propagation task and one for the IAC segmentation task. For this reason, a lot of code was duplicated and a single repository was created to host the whole codebase. Moreover, the code has been rewritten from scratch, and only some parts of the original codebase have been copied. Heavy use of the TorchIO library, maintained by Perez Garcia [33], has been made to simplify and optimize part of the pipeline.

### 4.3.1 Data Loading

The first issue tackled was the lack of use of TorchIO classes as an abstraction for the new proposed dataset. The original codebase was using a custom class that was responsible to load the data, compute some statistics, and reading part of the config file to select which transformation to apply to perform the data augmentation. Moreover, custom transformation functions were defined here in the same file.

One of the main advantages of using TorchIO is that it provides three main data structures which are used to represent the data: *Image*, *Subject* and *SubjectsDataset*.

The *Image* class, representing one medical image, stores a 4D tensor, whose voxels encode, e.g., signal intensity or segmentation labels, and the corresponding affine transform, typically a rigid (Euclidean) transform, to convert voxel indices to world coordinates in mm. Arbitrary fields such as acquisition parameters may also be stored. Subclasses are used to indicate specific types of images, such as *ScalarImage* and *LabelMap*, which are used to store, e.g., CBCT scans and segmentations, respectively.

The *Subject* is a data structure used to store images associated with a subject and any other metadata necessary for processing. It is essential to link a *ScalarImage* to its relative *LabelMaps*.

The *SubjectsDataset* is a subclass of `torch.utils.data.Dataset` which is used to store a collection of *Subjects*. It can be used with PyTorch `DataLoader` for efficient loading and augmentation. The figure 4.1 depicts the relationship between these classes.

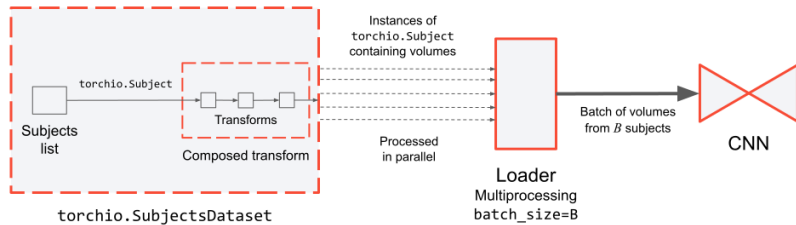


FIGURE 4.1: *SubjectsDataset* class and its relationships.

With these data structures, a `Maxillo` class, which inherit from `SubjectsDataset` has been created to load the data. This class takes as input the path of the dataset, which is split to load (train, validation, test, synthetic) and optionally a list of Transformations that must be used as data augmentations. This class is completely independent from the rest of the code, and thus can be used in any other project which requires loading the `Maxillo` dataset.

### 4.3.2 Data Augmentation

Transformation functions that were previously defined in the same file of the data loader have been moved to a new file. Some of them were already implemented inside TorchIO

and thus have been removed. The remaining ones have been adapted to inherit from the abstract class `torchio.transforms.Transform`, in order to be easily used inside TorchIO, such with the *Composability* method which allows creating a directed acyclic graph of transformations that must be applied to the data.

### 4.3.3 Config and command line arguments

In the original codebase, the parameters of the program were passed both as arguments from the command line and in the config file. This could generate some confusion and make it harder to reproduce experiments as the config file alone wasn't enough. For this reason, the config file is now the only source of parameters, while the only arguments that the software accepts are the path of the config file and a boolean value to enable/disable Tensorboard [34].

### 4.3.4 Interfaces

Something about interfaces used for Models, Losses, Optimizers, Schedulers and Experiments...

### 4.3.5 Deploying and Running

The code was managed using Git and the repository is hosted on GitHub the repository is public and can be found at [https://github.com/AImageLab-zip/alveolar\\_canal](https://github.com/AImageLab-zip/alveolar_canal). By using Git, it was possible to easily deploy the code on the AImageLab Server by means of a simple script that keeps the code up to date with the main branch. Other branches were used to develop new features and to test them before merging everything in the main branch. The Gitflow workflow was used to manage the branches. The training was scheduled using the SLURM scheduler [35], which is installed on the server. Some scripts were written to automatize the training process, which often required running sequentially multiple experiments with different configuration files and to recover training from a given checkpoint when the training was long and the scheduler kill the process for exceeding the time limit.

# Chapter 5

## Trying to improve the State of the Art

The architecture proposed by Cipriano *et al.* was quite simple yet effective. The main novel addition was the use of positional encoding. We now want to try to improve the results obtained by them by adding some more complex and more recent architectures, losses, and optimizers.

### 5.1 Boundary Loss

Jointly with PosPadUNet3D, standard DICE loss was used. We also tried to use CrossEntropy loss, but the results were not as good as with DICE loss so it has been discarded. As we were dealing with highly unbalanced data, less than 1% of the whole volume is the canal, we looked for alternative losses which deal with this problem.

Kervadec *et al.* [18] proposed a loss function that takes the form of a distance metric on the space of contours instead of regions. Dice or cross-entropy, are based on regional integrals, which are convenient for training deep neural networks. In practice, these regional integrals are summations over the segmentation regions of differentiable functions, each directly invoking the softmax probability outputs of the network. Therefore, standard stochastic optimizers such as SGD are directly applicable. Unfortunately, difficulties occur for highly unbalanced segmentations, for instance, when the size of the target foreground region is several orders of magnitude less than the background size, which is a common characteristic for medical images. The problem with such losses is that they assume identical importance distribution for all the samples and classes.

In the aforementioned paper, the authors proposed a new type of loss, named *Boundary loss* that aims to mitigate the issues related to regional losses in highly unbalanced segmentation problems. Rather than using unbalanced integrals over the regions, a boundary loss uses integrals over the boundary between the regions. Furthermore, it provides information that is complementary to regional losses. It is, however, challenging to represent the boundary points corresponding to the regional softmax outputs of a CNN. This difficulty may explain why boundary losses have been avoided in the context of deep segmentation networks.

### 5.1.1 Formulation

The Boundary loss has been formulated as follows: let  $I : \Omega \subset \mathbb{R}^{2,3} \rightarrow \mathbb{R}$  denotes an image with spatial domain  $\Omega$ , and  $g : \Omega \rightarrow 0, 1$  a binary ground truth segmentation of the image such that  $g(p) = 1$  if the pixel  $p$  belongs to the target region  $G \subset \Omega$  and 0 otherwise. Let  $s_\theta : \Omega \rightarrow [0, 1]$  denotes the softmax probability output of a deep segmentation network, and  $S_\theta \subset \Omega$  denotes the corresponding segmentation region:  $\S_\theta = p \in \Omega | s_\theta(p) >= \delta$  for some threshold  $\delta$ . Let  $\Delta G$  denote a representation of the boundary of the ground-truth region  $G$  (i.e. the set of points of  $G$ , which have a spatial neighbor in background  $\Omega \setminus G$ ) and  $\Delta S_\theta$  denoting the boundary of the segmentation region defined by the network output.

The boundary loss can now be defined as:

$$\mathcal{L}_{\text{boundary}}(\theta) = \int_{\Omega} \phi_G(q) s_\theta(q) dq \quad (5.1)$$

Where  $\phi_G$  is the level set of the ground-truth region  $G$ , obtained by using the signed distance transform over  $G$ .

### 5.1.2 Combining with other loss functions

As we have already said, this type of loss is complementary to the regional losses, since it provides information about the boundary of the segmentation region, therefore they can be combined. In our experiments, we used the following combination:

$$\mathcal{L}(\theta) = (1 - \alpha)\mathcal{L}_{\text{boundary}}(\theta) + \alpha\mathcal{L}_{\text{DICE}}(\theta) \quad (5.2)$$

Where  $\alpha$  is a hyperparameter that weights the two losses.

Kervadec *et al.* [18] in the paper where they presented this type of novel loss they've adopted a peculiar way to set this  $\alpha$ . As the training was kind of unstable they set  $\alpha$  to an initial value of 0 and increased its value by 0.01 and each training epoch until a fixed threshold. This type of approach have given the best results in terms of stability and performance thus we decided to adopt it also in our experiments.

## 5.2 PosDeepLab v3+

DeepLab v3+ is another well-known architecture for semantic segmentation. It was proposed by Chen *et al.* in 2015 with version 1 [36]. Later in the years, they proposed small changes to the architecture, which resulted in version 2 [37], 3 [38], and the latest one, version 3+ [39]. The main novelty that can be found in this architecture is the use of Atrous Spatial Pyramid Convolutions, which are dilated convolutions in parallel, each one with a different dilation rate and later concatenated, the use of a fully connected Conditional Random Field, which improves the segmentation by maximizing the label agreement between similar pixels, and the use of depth-wise separable convolutions, which are a way to reduce the number of parameters in the network. The model architecture is shown in Figure 5.1.

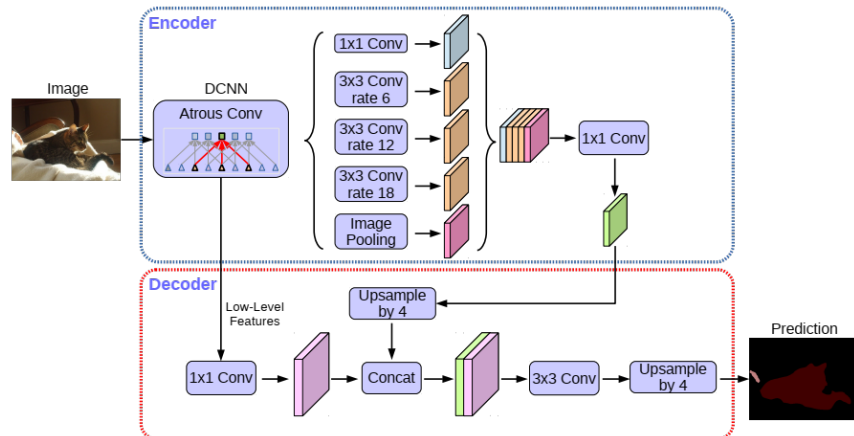


FIGURE 5.1: DeepLab v3+ architecture

### 5.3 PosSegNet

SegNet is a fully convolutional network for semantic segmentation. It was proposed by Badrinarayanan *et al.* [40] in 2015 and is structured in two parts: an encoder and a decoder, similar to the one used in the U-Net. While the encoder is made of convolutional layers followed by max pooling. The indices of the max pooling are stored to be used in the decoder during the upsampling. The encoder part is made of the 13 convolutional layers of the VGG16 network, while in the decoder always 13 layers are used, but they are made of transposed convolutional layers. Finally, a K-class softmax classifier is used to predict the class for each pixel. Also in this case the same positional encoding used in PosPadUNet3D was introduced, thus named the new network PosSegNet, as it was shown to be effective in the previous architecture. SegNet was originally proposed for the segmentation of images, but by changing the 2D operations to 3D ones, it can be used for the segmentation of 3D volumes. The architecture is shown in figure 5.2.

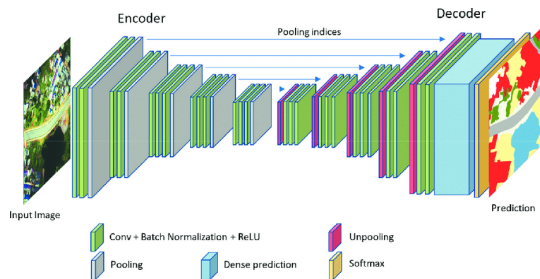


FIGURE 5.2: SegNet architecture

### 5.4 SwinUNETR3D

Hatamizadeh *et al.* [41, 42] recently proposed a novel architectures for 3D medical image segmentation which make use of the Transformer architecture. The main idea is to replace the convolutions of U-Net used in the encoding phase with Transformers. Instead of the standard Vision Transformers, Swin Transformers have been used as they have shown better performance on images. As Transformers are known to suffer where there is a lack of data, also a pre-training procedure has been proposed [22] to overcome this problem. In the following sections, we will describe SwinUNETR, starting from the standard Transformer as proposed in the original paper "*Attention is all you need*" by Vaswani *et al.* [43], and

then we will look at how these ideas have been moved from Natural Language Processing to Computer Vision.

### 5.4.1 Transformer Architecture

The transformer architecture was first introduced by Vaswani *et al.* [43] in 2017 in the field of Natural Language Processing. The main idea is to replace a recurrent layer with a multi-head attention mechanism, which is a linear operation that can be computed in parallel. The attention mechanism is computed as follows:

$$\text{Attention}(Q, K, V) = \text{softmax}\left(\frac{QK^T}{\sqrt{d_k}}\right)V \quad (5.3)$$

Where  $Q \in \mathbb{R}^{d_k}$  is the query,  $K \in \mathbb{R}^{d_k}$  is the key and  $V \in \mathbb{R}^{d_v}$  is the value. If we would like to make it multi-head, we add more attention layers in parallel and concatenate the results. The final output of a multi-head attention layer is computed as follows:

$$\text{MultiHeadAttention}(Q, K, V) = \text{Concat}(\text{head}_1, \dots, \text{head}_h)W^O \quad (5.4)$$

where  $\text{head}_i = \text{Attention}(QW_i^Q, KW_i^K, VW_i^V)$ . The projection matrices  $W_i^Q \in \mathbb{R}^{d_{\text{model}} \times d_k}$ ,  $W_i^K \in \mathbb{R}^{d_{\text{model}} \times d_k}$ ,  $W_i^V \in \mathbb{R}^{d_{\text{model}} \times d_v}$ , and  $W^O \in \mathbb{R}^{hdv \times d_{\text{model}}}$  are learned parameters. The complete architecture, which also adds a residual connection, a linear layer, and a normalization layer, is shown in Figure 5.3.

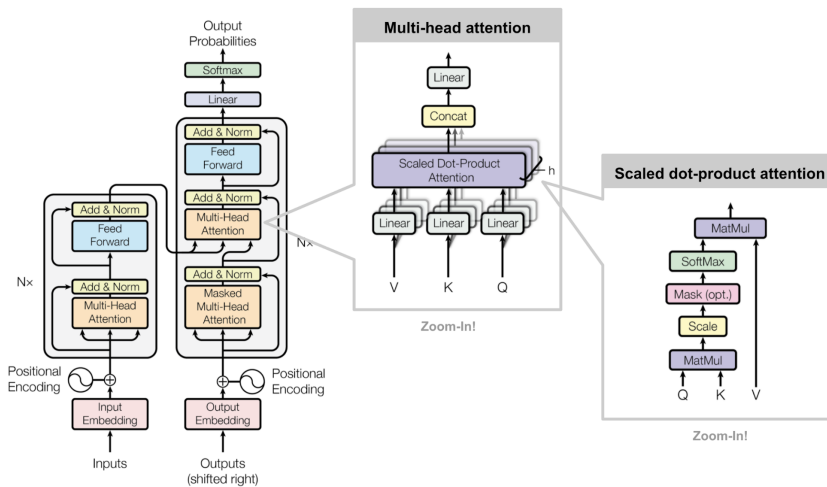


FIGURE 5.3: Transformer architecture

### 5.4.2 Vision Transformer

While the Transformer architecture has become the de-facto standard for natural language processing tasks, its applications to computer vision have remained limited for a few years. One of the reasons is that the complexity of the attention mechanism is  $O(n^2)$ , where  $n$  is the number of pixels in the image. This makes it impractical for medium and large-size images. In 2020, Dosovitskiy *et al.* [28] proposed a novel architecture called Vision Transformer (ViT) which is able to scale up the Transformer architecture to images. The main idea is to reshape the original image  $x \in \mathbb{R}^{H \times W \times C}$  into a sequence of patches  $x_p \in \mathbb{R}^{P \times P \times C}$ , where  $H$ ,  $W$ ,  $C$  and  $P$  are the height, width, number of channels and resolution of patches respectively. The Transformer uses constant latent vector size  $D$  through all of its layers, so we flatten the patches and map to  $D$  dimensions with a trainable linear projection. The outputs of such projections are patch embeddings. An additional token [class] is added to the sequence, which is used to encode the class label of the image. The whole architecture is depicted in Figure 5.4.

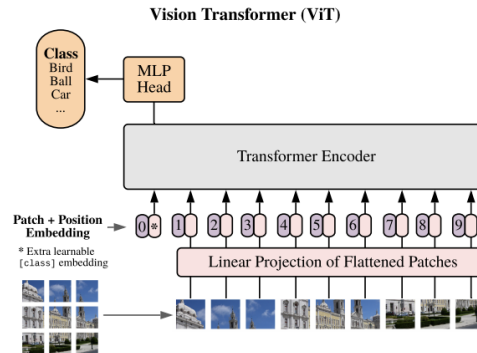


FIGURE 5.4: Vision Transformer architecture

### 5.4.3 Swin Transformer

Swin Transformer, where the word *Swin* stands for *Shifted Window*, is a novel architecture proposed by Liu *et al.* [44] in 2021 which has become quite popular in the field of computer vision in these latter years. The problem that the authors wanted to solve is that the Vision Transformers are not really well suited for tasks that require dense prediction at pixel level such as semantic segmentation, so they propose a novel that constructs hierarchical feature maps and has linear computational complexity to image size.

The Swin Transformer still relies on patches, but instead of choosing one size and sticking with it, it first starts with small patches for the first Transformer layer, then merges them into bigger ones in the deeper Transformer layers. The first size chosen for the patches is  $4 \times 4$  and then it is projected to a chosen dimensionality  $C$ , which in the paper has been proposed to be 96 for the small model and 192 for the large model. Then, these vectors are processed with a Transformer which makes use of a Shifted Window based Self-Attention, introduced in this paper, instead of the classical Self-Attention used in ViT. This type of attention has the benefit to be linear because it is limited to a fixed number of patches  $M$ , so its complexity will be  $O(M \times N)$  instead of  $O(N^2)$  where  $N$  is the number of patches.

The output of such Transformer Layer is fed into a Merging Layer which concatenates the vectors of groups of  $2 \times 2$  neighboring patches and fed to another Linear layer to reduce the dimensionality. This process is repeated but for each layer, the region where the attention was limited to is shifted in order to apply the attention to a different set of patches, which before could not be seen among each other.

As a result, Swin Transformers are suitable for various downstream tasks wherein the extracted multi-scale features can be leveraged for further processing.

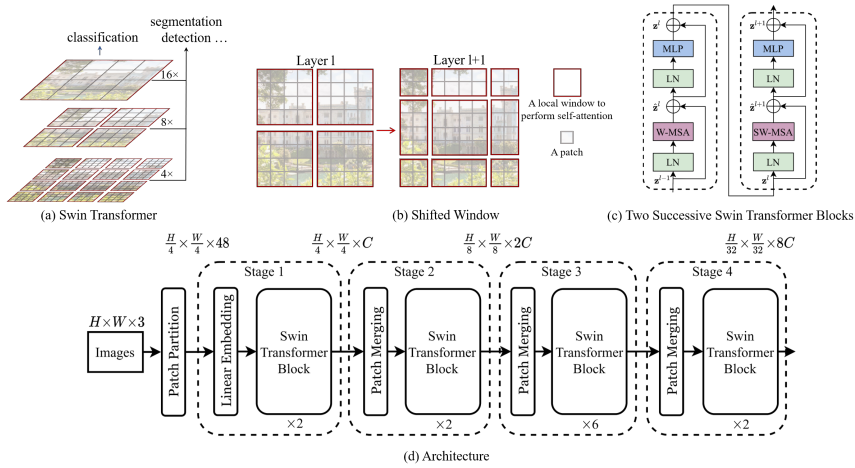


FIGURE 5.5: Swin Transformer components

#### 5.4.4 Final Architecture and pre-training

The final architecture that has been proposed by Hatamizadeh *et al.* [42] follows the structure of U-Net3D, but in the encoder part, SwinTransformers are used instead of the standard 3D

Convolution. Some changes from the original paper have been made in order to adapt the model to our type of data. From the original volume of size  $168 \times 280 \times 360$ , we extract patches of size  $96 \times 96 \times 96$ . These patches are fed in the SwinUNetr model which is composed of a 4-stages Swin Transformer that acts as the encoder part and a sequence of transposed convolutions as the decoder. For each stage of the encoder part, a skip connection is added to the output of the decoder stage with the same shape, as in the original U-Net architecture. The whole architecture is shown in Figure 5.6.

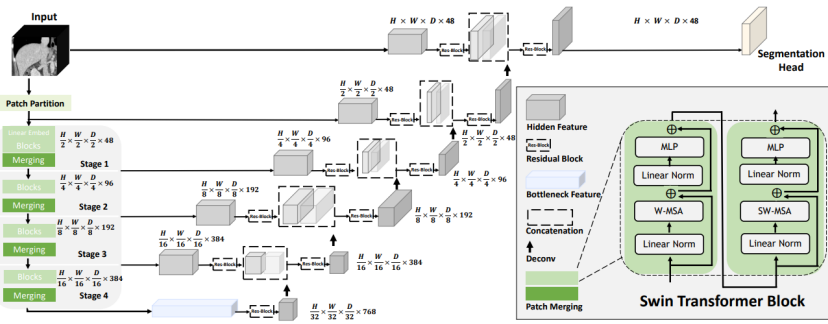


FIGURE 5.6: SwinUNETR architecture

As already mentioned, a pre-training phase is performed to overcome the data hungriness characteristic of Transformers. The pretraining has been performed by paper authors on a variety of datasets of CT scans of different types have been used. A total of 5 public CT datasets, consisting of a total of 5050 subjects, are used to construct the pre-training dataset. We do not have tried to perform the same pre-training on CBCT data instead of CT because the time required was prohibitive. The datasets used are:

- **Head & Neck Squamous Cell Carcinoma (HNSCC):** A collection contains imaging, radiation therapy, and clinical data from 627 head and neck squamous cell carcinoma (HNSCC) patients at MD Anderson Cancer Center. [45]
- **Lung Nodule Analysis 2016 (LUNA 16):** a collection of 888 CT scans of lung nodules. [46]
- **TCIA CT Colonography Trial:** a collection of 825 CT colonography scans. [47]
- **TCIA Covid 19:** a set of 2 datasets for a total of 753 CT scans of the chest and annotation about the Covid-19 infection. [48]
- **TCIA LIDC-IDRI:** a collection obtained by the collaboration of seven academic centers and eight medical imaging companies. It contains 1018 cases of diagnostic and

lung cancer screening thoracic computed tomography (CT) scans with marked-up annotated lesions. [49]

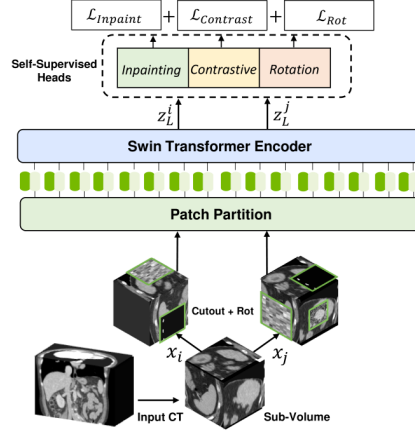


FIGURE 5.7: Pre-training phase

Multiple proxy tasks and formulated with a multi-objective loss function has been used in that self-supervised phase:

- **Inpainting:** a transposed convolution layer have been attached to the encoder as reconstruction head, a patch is removed from the original volume and the model must manage to reconstruct the missing voxels, standard L1 loss

$$\mathcal{L}_{inpaint} = \|\mathcal{X} - \hat{\mathcal{X}}\|_1$$

is used, where  $\hat{\mathcal{X}}$  is the output of the model and  $\mathcal{X}$  is the ground truth.

- **Image rotation:** The rotation prediction task predicts the angle categories by which the input sub-volume is rotated. For simplicity, we employ  $R$  classes of 0, 90, 180, and 270 rotations along the z-axis. An MLP classification head is used for predicting the softmax probabilities  $\hat{y}_r$  of rotation categories. Given the ground truth  $y_r$ , a cross-entropy loss is used for rotation prediction task:

$$\mathcal{L}_{rot} = - \sum_{r=1}^R y_r \log(\hat{y}_r)$$

- **Contrastive coding:** The rotations used above where also used inside a contrastive loss [50]. Given a batch of augmented sub-volumes, the contrastive coding allows

for a better representation learning by maximizing the mutual information between positive pairs, while minimizing that between negative pairs. A linear layer is attached to the encoder to map each augmented sub-volume to a latent representation  $v$ . The cosine similarity is used as the distance measurement. The final loss between a pair  $v_i$  and  $v_j$  is defined as:

$$\mathcal{L}_{contra} = -\log \frac{\exp(sim(v_i, v_j)/t)}{\sum_k^{2N} 1_{k \neq i} \exp(sim(v_i, v_k)/t)}$$

where  $t$  is the measurement of normalized temperature scale.  $1$  is the indicator function evaluating to  $1 \iff k \neq i$ , and  $sim(\cdot, \cdot)$  denotes the dot product between normalized embeddings. The contrastive learning loss function has been shown to strengthens the intra-class compactness as well as the inter-class separability.

In conclusion, we minimize the final loss that is the sum of these 3 losses:

$$\mathcal{L} = \lambda_1 \mathcal{L}_{inpaint} + \lambda_2 \mathcal{L}_{rot} + \lambda_3 \mathcal{L}_{contra}$$

Where  $\lambda_1$ ,  $\lambda_2$  and  $\lambda_3$  are the weights of the 3 losses and are set to 1 as experimentally shown to be the optimal value. In the Figure 5.7 this process is visually represented.

## 5.5 Hann window function

By looking at the whole segmented volume, we noticed that when using PosPadUNet3D, the segmentation was not very accurate in the borders of each patch. In order to solve this problem, we decided to extract overlapping patches from the original volume instead of the non-overlapping method used in the original paper. When two patches overlap, we would like to compute a weighted average based on the distance from the center. TODO: explain what happen in audio. For this reason, we decided to apply the Hann window function to 3D volumes to try to reduce edge effects.

### 5.5.1 Hann window function in 1D

The Hann window function, named after Julius von Hann, has been first defined in the field of signal processing [50], thus in 1D, as:

$$w[n] = 0.5(1 - \cos(\frac{2\pi n}{N})), \quad n = 0, \dots, N$$

where  $x$  is the index of the window and  $N$  is the total number of samples. This function is symmetric, with a maximum value of 1 in the middle of the window and a minimum value of 0 at the edges. Another interesting property is that the sum of two Hann windows shifted by  $\frac{N}{2}$  is equal to a rectangular window of width  $N$  and height 1:

$$w[n] + w[n + N] = 0.5(1 - \cos(\frac{2\pi n}{N})) + 0.5(1 - \cos(\frac{2\pi(n + N)}{N})) = 1 \quad (5.5)$$

### 5.5.2 Hann window function in 3D

To apply the Hann window function in 3D, we simply apply the 1D function to each dimension of the volume:

$$w[x, y, z] = w[x]w[y]w[z] \quad (5.6)$$

but we have to handle the case where the patch is close to the border of the original volume. Here the patch is overlapped only on a part of the volume, thus the window function must be adapted accordingly. In the 3D case, 27 different cases can occur, depending on the position of the patch in the original volume. In Figure 5.8 all the 9 cases in the 2D scenario are shown. Mathematically, this would require to define many different functions and being unable to efficiently implement in Python the  $N$ -dimensional case, with  $N$  as a parameter.

### 5.5.3 Implementation

The first step is to generate a  $N$ -dim Hann window, by starting from a 1-dim window. Here we use the method provided in the PyTorch library `torch.hann_window()`. To produce a 2-dim window, it is possible to exploit the broadcast property of tensors by multiplying a 1-dim window with shape  $(N, 1)$  with a 1-dim window with shape  $(1, N)$ , resulting in a 2-dim window with shape  $(N, N)$ . This process can be repeated to generate up to a  $N$ -dim window. The code is shown in Listing 5.1.

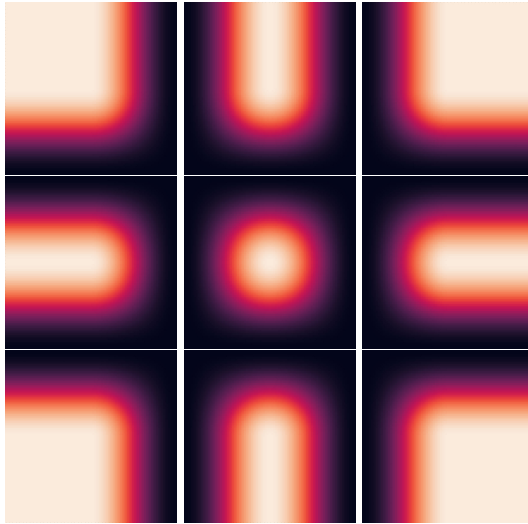


FIGURE 5.8: Different Hann window functions in 2D based on the position of the extracted patch.

---

```

def _get_hann_window(patch_size):
    hann_window_nd = torch.as_tensor([1])
    # create a n-dim hann window
    for spatial_dim, size in enumerate(patch_size):
        window_shape = np.ones_like(patch_size)
        window_shape[spatial_dim] = size
        hann_window_1d = torch.hann_window(
            size + 2,
            periodic=False,
        )
        hann_window_1d = hann_window_1d[1:-1].view(*window_shape)
    hann_window_nd = hann_window_nd * hann_window_1d
    return hann_window_nd

```

---

LISTING 5.1: Python code to generate a  $N$ -dim Hann window

Once a  $N$ -dim Hann window is generated, the next step is to apply it to the predicted segmentation and, to avoid small numerical errors, we save the coefficients used in a tensor of the same shape of the segmentation. These numerical errors are due to the fact that these Hann windows are discrete and not continuous, thus the sum of the window coefficients is not always equal to 1. Moreover this approach to avoid us to craft a specific window tensor

for each case near the border, which would become impractical for high dimensional cases. The code is shown in Listing 5.2.

---

```
hann_window = _get_hann_window(patch_size)
for patch, location in zip(batch, locations):
    i_ini, j_ini, k_ini, i_fin, j_fin, k_fin = location

    patch = patch * _hann_window
    _output_tensor[
        :,
        i_ini:i_fin,
        j_ini:j_fin,
        k_ini:k_fin,
    ] += patch
    _avgmask_tensor[
        :,
        i_ini:i_fin,
        j_ini:j_fin,
        k_ini:k_fin,
    ] += _hann_window
```

---

LISTING 5.2: Code to apply Hann window to a batch of patches given their locations

Once the segmentation for the whole volume is computed, the final step is to divide the output tensor by the average mask tensor, to obtain the final segmentation. The code is shown in Listing 5.3.

---

```
_output_tensor = _output_tensor / _avgmask_tensor
```

---

LISTING 5.3: Code to compute the final segmentation

This method has been successfully implemented to TorchIO library and is available since version 0.18.83. The code is available at <https://github.com/fepegar/torchio/blob/main/src/torchio/data/inference/aggregator.py>.

## 5.6 Performance improvements

The last attempt made aimed to improve the performance of the model without a excessive drop in the metrics. Being that the face of a person is symmetrical, we decided to crop each volume in two halves, and flip the right one, then we trained the model on both halves separately. Moreover, as there is a considerable space between the two halves, we managed to crop a little bit more of data while leaving the canals still intact. We also wanted to be able to feed a single volume into the network without having to extract smaller patches from it. To do so, we resize the original volume by a factor of 3. Once a resized volume is fed in the network, we could resize them back to the original size and compute the metrics as usual. With this approach, we managed to gain a speedup of 24 times, while the DICE score was only slightly affected by a drop of 0.02.

## 5.7 Results

All the models have been trained using PyTorch [51], on two NVIDIA P100 GPUs with 16 GB of memory, over the AImagelab server. The model proposed by Cipriano *et al.* achieved the best results among the different tries and managed to keep the title of the state-of-the-art model for the task of segmentation of the Inferior Alveolar Canal. However, the experiments that have been made have obtained comparable metrics thus they might open a new path to follow to improve such results.

# **Chapter 6**

## **Conclusions and future work**

### **6.1 Conclusion**

The work described in this thesis has been concerned with the analysis of extremely novel techniques for the segmentation of 3D medical images, applied to our specific problem of segmenting the Inferior Alveolar Canal (IAC) in cone-beam CT (CBCT) images. After presenting the state-of-the-art in the field of image segmentation, the work focused on improving the already existing codebase of PosPadUNet3D by making the code more maintainable, optimizing some process of the pipeline and by adding new features. Finally, novel architecture proposed were implemented using PyTorch and TorchIO, even from scratch when no code were provided in the relative paper, tested and compared with the work carried out by Cipriano *et al.* .

Even if no substantial improvement regarding the metrics has been made, this work resulted in a improvement of the code for future work and in a contribution to the TorchIO library.

### **6.2 Recommendation for Future Work**

All the segmentation outputs that we've got with the tested networks had in common the lack of being a single tube for each canal that we wanted to segment. This problem can be overcome by using shape model and asking to the network to output the parameters for such model instead of a  $H \times W \times D$  segmentation map. Some novel loss that care about the

topology of the output have been proposed, but has not been yet widely used by the research community and hence it has not been a priority to try during this work. Lastly, transformers are always being more and more popular in the field of computer vision hence the results we've got with our tests can still have some room for improvements by getting inspired by novel approach used also in other field such as NLP.

# Bibliography

- [1] Dale Miles and Robert Danforth. A clinician’s guide to understanding cone beam volumetric imaging (cbvi). *Acad Dent Ther Stomatol*, pages 1–13, 01 2007.
- [2] Olaf Ronneberger, Philipp Fischer, and Thomas Brox. U-net: Convolutional networks for biomedical image segmentation, 2015.
- [3] Özgün Çiçek, Ahmed Abdulkadir, Soeren S Lienkamp, Thomas Brox, and Olaf Ronneberger. 3d u-net: learning dense volumetric segmentation from sparse annotation. In *International conference on medical image computing and computer-assisted intervention*, pages 424–432. Springer, 2016.
- [4] Fausto Milletari, Nassir Navab, and Seyed-Ahmad Ahmadi. V-net: Fully convolutional neural networks for volumetric medical image segmentation. In *2016 fourth international conference on 3D vision (3DV)*, pages 565–571. IEEE, 2016.
- [5] Yang Gao, Jeff M Phillips, Yan Zheng, Renqiang Min, P Thomas Fletcher, and Guido Gerig. Fully convolutional structured lstm networks for joint 4d medical image segmentation. In *2018 IEEE 15th International Symposium on Biomedical Imaging (ISBI 2018)*, pages 1104–1108. IEEE, 2018.
- [6] Minh H Vu, Guus Grimbergen, Tufve Nyholm, and Tommy Löfstedt. Evaluation of multislice inputs to convolutional neural networks for medical image segmentation. *Medical Physics*, 47(12):6216–6231, 2020.
- [7] Ian Goodfellow, Jean Pouget-Abadie, Mehdi Mirza, Bing Xu, David Warde-Farley, Sherjil Ozair, Aaron Courville, and Yoshua Bengio. Generative adversarial networks. *Communications of the ACM*, 63(11):139–144, 2020.

- [8] Federico Pollastri, Federico Bolelli, Roberto Paredes, and Costantino Grana. Augmenting data with gans to segment melanoma skin lesions. *Multimedia Tools and Applications*, 79(21):15575–15592, 2020.
- [9] Ozan Oktay, Enzo Ferrante, Konstantinos Kamnitsas, Mattias Heinrich, Wenjia Bai, Jose Caballero, Stuart A Cook, Antonio De Marvao, Timothy Dawes, Declan P O’Regan, et al. Anatomically constrained neural networks (acnns): application to cardiac image enhancement and segmentation. *IEEE transactions on medical imaging*, 37(2):384–395, 2017.
- [10] Steven Guan, Amir A Khan, Siddhartha Sikdar, and Parag V Chitnis. Fully dense unet for 2-d sparse photoacoustic tomography artifact removal. *IEEE journal of biomedical and health informatics*, 24(2):568–576, 2019.
- [11] Christian Szegedy, Wei Liu, Yangqing Jia, Pierre Sermanet, Scott Reed, Dragomir Anguelov, Dumitru Erhan, Vincent Vanhoucke, and Andrew Rabinovich. Going deeper with convolutions. In *Proceedings of the IEEE conference on computer vision and pattern recognition*, pages 1–9, 2015.
- [12] Christian Szegedy, Vincent Vanhoucke, Sergey Ioffe, Jon Shlens, and Zbigniew Wojna. Rethinking the inception architecture for computer vision. In *Proceedings of the IEEE conference on computer vision and pattern recognition*, pages 2818–2826, 2016.
- [13] Andrew G Howard, Menglong Zhu, Bo Chen, Dmitry Kalenichenko, Weijun Wang, Tobias Weyand, Marco Andreetto, and Hartwig Adam. Mobilenets: Efficient convolutional neural networks for mobile vision applications. *arXiv preprint arXiv:1704.04861*, 2017.
- [14] Ozan Oktay, Jo Schlemper, Loic Le Folgoc, Matthew Lee, Mattias Heinrich, Kazunari Misawa, Kensaku Mori, Steven McDonagh, Nils Y Hammerla, Bernhard Kainz, et al. Attention u-net: Learning where to look for the pancreas. *arXiv preprint arXiv:1804.03999*, 2018.
- [15] Jie Hu, Li Shen, and Gang Sun. Squeeze-and-excitation networks. In *Proceedings of the IEEE conference on computer vision and pattern recognition*, pages 7132–7141, 2018.
- [16] Jonathan Long, Evan Shelhamer, and Trevor Darrell. Fully convolutional networks for semantic segmentation. In *Proceedings of the IEEE conference on computer vision and pattern recognition*, pages 3431–3440, 2015.

- [17] Carole H Sudre, Wenqi Li, Tom Vercauteren, Sebastien Ourselin, and M Jorge Cardoso. Generalised dice overlap as a deep learning loss function for highly unbalanced segmentations. In *Deep learning in medical image analysis and multimodal learning for clinical decision support*, pages 240–248. Springer, 2017.
- [18] Hoel Kervadec, Jihene Bouchtiba, Christian Desrosiers, Eric Granger, Jose Dolz, and Ismail Ben Ayed. Boundary loss for highly unbalanced segmentation. In *International conference on medical imaging with deep learning*, pages 285–296. PMLR, 2019.
- [19] Xiaomeng Li, Lequan Yu, Hao Chen, Chi-Wing Fu, Lei Xing, and Pheng-Ann Heng. Transformation-consistent self-ensembling model for semisupervised medical image segmentation. *IEEE Transactions on Neural Networks and Learning Systems*, 32(2):523–534, 2020.
- [20] Davood Karimi and Septimiu E Salcudean. Reducing the hausdorff distance in medical image segmentation with convolutional neural networks. *IEEE Transactions on medical imaging*, 39(2):499–513, 2019.
- [21] Marco Cipriano, Stefano Allegretti, Federico Bolelli, Federico Pollastri, and Costantino Grana. Improving segmentation of the inferior alveolar nerve through deep label propagation. In *Proceedings of the IEEE/CVF Conference on Computer Vision and Pattern Recognition*, pages 21137–21146, 2022.
- [22] Yucheng Tang, Dong Yang, Wenqi Li, Holger R Roth, Bennett Landman, Daguang Xu, Vishwesh Nath, and Ali Hatamizadeh. Self-supervised pre-training of swin transformers for 3d medical image analysis. In *Proceedings of the IEEE/CVF Conference on Computer Vision and Pattern Recognition*, pages 20730–20740, 2022.
- [23] Thomas Elsken, Jan Hendrik Metzen, and Frank Hutter. Neural architecture search: A survey. *The Journal of Machine Learning Research*, 20(1):1997–2017, 2019.
- [24] Fabian Isensee, Jens Petersen, Andre Klein, David Zimmerer, Paul F Jaeger, Simon Kohl, Jakob Wassermann, Gregor Koehler, Tobias Norajitra, Sebastian Wirkert, et al. nnunet: Self-adapting framework for u-net-based medical image segmentation. *arXiv preprint arXiv:1809.10486*, 2018.
- [25] Hongyang Gao and Shuiwang Ji. Graph u-nets. In *international conference on machine learning*, pages 2083–2092. PMLR, 2019.

- [26] Han Yang, Xingjian Zhen, Ying Chi, Lei Zhang, and Xian-Sheng Hua. Cpr-gcn: Conditional partial-residual graph convolutional network in automated anatomical labeling of coronary arteries. In *Proceedings of the IEEE/CVF conference on computer vision and pattern recognition*, pages 3803–3811, 2020.
- [27] Jesse Sun, Fatemeh Darbehani, Mark Zaidi, and Bo Wang. Saunet: Shape attentive u-net for interpretable medical image segmentation. In *International Conference on Medical Image Computing and Computer-Assisted Intervention*, pages 797–806. Springer, 2020.
- [28] Alexey Dosovitskiy, Lucas Beyer, Alexander Kolesnikov, Dirk Weissenborn, Xiaohua Zhai, Thomas Unterthiner, Mostafa Dehghani, Matthias Minderer, Georg Heigold, Sylvain Gelly, et al. An image is worth 16x16 words: Transformers for image recognition at scale. *arXiv preprint arXiv:2010.11929*, 2020.
- [29] Jieneng Chen, Yongyi Lu, Qihang Yu, Xiangde Luo, Ehsan Adeli, Yan Wang, Le Lu, Alan L Yuille, and Yuyin Zhou. Transunet: Transformers make strong encoders for medical image segmentation. *arXiv preprint arXiv:2102.04306*, 2021.
- [30] Marco Cipriano, Stefano Allegretti, Federico Bolelli, Mattia Di Bartolomeo, Federico Pollastri, Arrigo Pellacani, Paolo Minafra, Alexandre Anesi, and Costantino Grana. Deep segmentation of the mandibular canal: a new 3d annotated dataset of cbct volumes. *IEEE Access*, 10:11500–11510, 2022.
- [31] Cristian Mercadante, Marco Cipriano, Federico Bolelli, Federico Pollastri, Alexandre Anesi, Costantino Grana, et al. A cone beam computed tomography annotation tool for automatic detection of the inferior alveolar nerve canal. In *16th International Conference on Computer Vision Theory and Applications-VISAPP 2021*, volume 4, pages 724–731. SciTePress, 2021.
- [32] Herbert Edelsbrunner, David Kirkpatrick, and Raimund Seidel. On the shape of a set of points in the plane. *IEEE Transactions on information theory*, 29(4):551–559, 1983.
- [33] Fernando Pérez-García, Rachel Sparks, and Sébastien Ourselin. Torchio: A python library for efficient loading, preprocessing, augmentation and patch-based sampling of medical images in deep learning. *Computer Methods and Programs in Biomedicine*, 208:106236, 2021. ISSN 0169-2607. doi: <https://doi.org/10.1016/j.cmpb.2021.106236>.

- [34] Martín Abadi, Ashish Agarwal, Paul Barham, Eugene Brevdo, Zhifeng Chen, Craig Citro, Greg Corrado, Andy Davis, Jeffrey Dean, et al. Tensorflow: Large-scale machine learning on heterogeneous distributed systems, 2015.
- [35] Andy B Yoo, Morris A Jette, and Mark Grondona. Slurm: Simple linux utility for resource management. In *Workshop on job scheduling strategies for parallel processing*, pages 44–60. Springer, 2003.
- [36] Liang-Chieh Chen, George Papandreou, Iasonas Kokkinos, Kevin Murphy, and Alan L Yuille. Semantic image segmentation with deep convolutional nets and fully connected crfs. *arXiv preprint arXiv:1412.7062*, 2014.
- [37] Liang-Chieh Chen, George Papandreou, Iasonas Kokkinos, Kevin Murphy, and Alan L Yuille. Deeplab: Semantic image segmentation with deep convolutional nets, atrous convolution, and fully connected crfs. *IEEE transactions on pattern analysis and machine intelligence*, 40(4):834–848, 2017.
- [38] Liang-Chieh Chen, George Papandreou, Florian Schroff, and Hartwig Adam. Rethinking atrous convolution for semantic image segmentation. *arXiv preprint arXiv:1706.05587*, 2017.
- [39] Liang-Chieh Chen, Yukun Zhu, George Papandreou, Florian Schroff, and Hartwig Adam. Encoder-decoder with atrous separable convolution for semantic image segmentation. In *Proceedings of the European conference on computer vision (ECCV)*, pages 801–818, 2018.
- [40] Vijay Badrinarayanan, Alex Kendall, and Roberto Cipolla. Segnet: A deep convolutional encoder-decoder architecture for image segmentation. *IEEE transactions on pattern analysis and machine intelligence*, 39(12):2481–2495, 2017.
- [41] Ali Hatamizadeh, Yucheng Tang, Vishwesh Nath, Dong Yang, Andriy Myronenko, Bennett Landman, Holger R Roth, and Daguang Xu. Unetr: Transformers for 3d medical image segmentation. In *Proceedings of the IEEE/CVF Winter Conference on Applications of Computer Vision*, pages 574–584, 2022.
- [42] Ali Hatamizadeh, Vishwesh Nath, Yucheng Tang, Dong Yang, Holger R Roth, and Daguang Xu. Swin unetr: Swin transformers for semantic segmentation of brain tumors in mri images. In *International MICCAI Brainlesion Workshop*, pages 272–284. Springer, 2022.

- [43] Ashish Vaswani, Noam Shazeer, Niki Parmar, Jakob Uszkoreit, Llion Jones, Aidan N Gomez, Łukasz Kaiser, and Illia Polosukhin. Attention is all you need. *Advances in neural information processing systems*, 30, 2017.
- [44] Ze Liu, Yutong Lin, Yue Cao, Han Hu, Yixuan Wei, Zheng Zhang, Stephen Lin, and Baining Guo. Swin transformer: Hierarchical vision transformer using shifted windows. In *Proceedings of the IEEE/CVF International Conference on Computer Vision*, pages 10012–10022, 2021.
- [45] Aaron J Grossberg, Abdallah SR Mohamed, Hesham Elhalawani, William C Bennett, Kirk E Smith, Tracy S Nolan, Bowman Williams, Sasikarn Chamchod, Jolien Heukelom, Michael E Kantor, et al. Imaging and clinical data archive for head and neck squamous cell carcinoma patients treated with radiotherapy. *Scientific data*, 5(1):1–10, 2018.
- [46] Arnaud Arindra Adiyoso Setio, Alberto Traverso, Thomas De Bel, Moira SN Berens, Cas Van Den Bogaard, Piergiorgio Cerello, Hao Chen, Qi Dou, Maria Evelina Fantacci, Bram Geurts, et al. Validation, comparison, and combination of algorithms for automatic detection of pulmonary nodules in computed tomography images: the luna16 challenge. *Medical image analysis*, 42:1–13, 2017.
- [47] C Daniel Johnson, Mei-Hsiu Chen, Alicia Y Toledano, Jay P Heiken, Abraham Dachman, Mark D Kuo, Christine O Menias, Betina Siewert, Jugesh I Cheema, Richard G Obregon, et al. Accuracy of ct colonography for detection of large adenomas and cancers. *New England Journal of Medicine*, 359(12):1207–1217, 2008.
- [48] Shivang Desai, Ahmad Baghal, Thidathip Wongsurawat, Piroon Jenjaroenpun, Thomas Powell, Shaymaa Al-Shukri, Kim Gates, Phillip Farmer, Michael Rutherford, Geri Blake, et al. Chest imaging representing a covid-19 positive rural us population. *Scientific data*, 7(1):1–6, 2020.
- [49] Samuel G Armato III, Geoffrey McLennan, Luc Bidaut, Michael F McNitt-Gray, Charles R Meyer, Anthony P Reeves, Binsheng Zhao, Denise R Aberle, Claudia I Henschke, Eric A Hoffman, et al. The lung image database consortium (lidc) and image database resource initiative (idri): a completed reference database of lung nodules on ct scans. *Medical physics*, 38(2):915–931, 2011.
- [50] Aaron van den Oord, Yazhe Li, and Oriol Vinyals. Representation learning with contrastive predictive coding. *arXiv preprint arXiv:1807.03748*, 2018.

- [51] Adam Paszke, Sam Gross, Francisco Massa, Adam Lerer, James Bradbury, Gregory Chanan, Trevor Killeen, Zeming Lin, Natalia Gimelshein, Luca Antiga, et al. Pytorch: An imperative style, high-performance deep learning library. *Advances in neural information processing systems*, 32, 2019.